ACS APPLIED MATERIALS & INTERFACES

Open Access

This article is licensed under CC-BY 4.0

www.acsami.org

Research Article

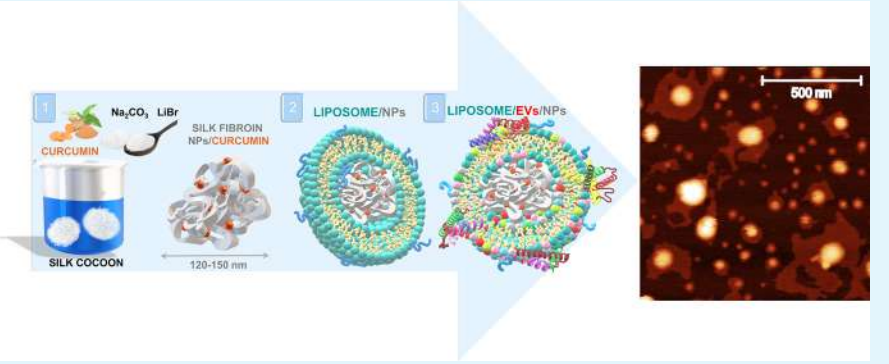
Silk Fibroin Nanoparticles Coated with an Extracellular Vesicle–Liposome Hybrid Shell for Controlled Cargo Delivery

Luca Randi,[$] Anastasiia Murmiliuk,[$1] Elia Bari, Laura Catenacci, Milena Sorrenti, Guillaume Gilliard,[4] Alice Piccinini,[3] Gouranga Manna, Clement Blanchet, Melissa Ann Gräwert, Aleksi Sutinen, Baohu Wu, Luca Puricelli, Loredana Casalis, Maria Cristina Bonferoni, Sara Perteghella,* and Valeria Rondelli*

Cite This: https://doi.org/10.1021/acsami.6c16066

Read Online

ACCESS | Metrics & More | Article Recommendations | Supporting Information



ABSTRACT: Silk fibroin nanoparticles (SFNPs) are promising nanocarriers for drug delivery owing to their biocompatibility, bioactivity, controllable biodegradability, and low toxicity. However, their translation is limited by formulation-dependent variations in morphology, colloidal stability, drug loading, and aggregation, all of which can affect release behavior and biological performance. Here, we investigated how fibroin solubilization conditions govern the self-assembly, internal structure, surface properties, and cargo delivery performance of SFNPs, using curcumin as a hydrophobic model compound. SFNPs were prepared by lithium bromide (LiBr) solubilization followed by desolvation and were characterized using complementary scattering, microscopy, and spectroscopy techniques. Fibroin solubilization temperature and curcumin loading modulated SFNP size, internal organization, and surface roughness. In particular, SFNPs formed 70–150 nm mass-fractal aggregates composed of smaller primary nanoparticles, and this morphology affected cargo loading and release by controlling accessible internal surface area and solvent contact. To further stabilize the system and engineer the external interface, SFNPs were incorporated into a liposome/extracellular vesicle (EV) hybrid shell by sonication, generating a carrier-in-carrier system containing EV-derived membrane-associated components. The hybrid lipid–EV/SFNP platform reduced aggregation in aqueous media and provided a tunable external shell for controlled release of hydrophobic cargo. Overall, this work establishes a structure-based proof of concept connecting upstream solubilization parameters to downstream nanoparticle architecture, supporting the rational design of hybrid silk-based nanocarriers for cargo delivery.

KEYWORDS: *silk fibroin, nanoparticles, SAXS, AF4-MALS, curcumin, hybrid nanocarriers*

INTRODUCTION

Nanoparticles (NPs) are widely studied as drug delivery systems due to their ability to protect therapeutic agents, control release profiles, and promote cell interaction. Among them, polymeric and protein nanoparticles have attracted particular interest because of their tunable physicochemical properties, stimuli-responsive behavior, and versatility in surface functionalization. Protein-based nanoparticles enable the design of biocompatible nanocarriers for targeted delivery and controlled release of proteins as well as of low-molecular-weight drugs.[1−4] Such protein-based nanoparticles often have a tendency toward uncontrolled aggregation and formation of larger clusters, resulting in broad particle size distribution and reduced batch-to-batch reproducibility. Therefore, careful optimization and strict control of the preparation protocol are required to obtain stable and reproducible nanoparticles.

Received: August 4, 2026
Revised: October 19, 2026
Accepted: October 28, 2026

Downloaded from pubs.acs.org/aamick/article-pdf/doi/10.1021/acsami.6c16066/6193937/am-2026-160662.pdf by guest on 15 November 2026

© XXXX The Author(s). Published by American Chemical Society

Silk Fibroin (SF), derived from *Bombyx mori* cocoons, can adopt distinct structural forms (Silk I, Silk II, and Silk III). Silk I is a hydrated, metastable conformation containing α-helical domains mixed with random coils and β-turns, whereas Silk II is characterized by an antiparallel β-sheet, resulting in a more crystalline and insoluble structure. Silk III is defined as a three-fold helical crystalline structure, characterized by an almost hexagonal structure and principally found in air-water interface.[4] The Silk I → Silk II transition is central to fiber formation and is also relevant for SF processing into biomaterials.[3,5] After sericin removal by degumming, fibroin can undergo Silk I/Silk II transitions depending on processing conditions, including exposure to organic solvents, high ionic strength, concentrated neutral salts, and salt–alcohol mixtures.[6]

The characteristic properties of SFNPs, such as low immunogenicity, targeted delivery potential, and controlled release capabilities, make them an attractive option for advancing drug delivery applications.[7] Recent studies have shown that SFNPs can be tailored in size, morphology, and surface properties to meet specific application needs.[8,9] Despite their promising features, conventional SFNPs produced by desolvation often suffer from significant drawbacks that limit their clinical translation; these include a lack of specific surface cues to escape immune recognition.[10] Furthermore, the internal nanostructure of SFNPs is frequently treated as a 'black box', with little attention paid to how the initial regeneration steps of the silk protein influence the final assembly and drug-carrier interactions.

This study was designed as a sequential process-structure-interface investigation: first, SFNP formation and curcumin loading were controlled through fibroin solubilization conditions; second, the optimized SFNPs were incorporated into a lipid shell; finally, EV-derived components were introduced to tune the external membrane interface. We systematically investigated how fibroin solubilization conditions (9.3 M LiBr,[11] varying temperature, and time) influence the physicochemical properties and aggregation state of the resulting SFNPs (graphical abstract). Curcumin was selected as a hydrophobic model bioactive compound to assess loading and in vitro release kinetics, addressing key limitations that hinder its therapeutic translation. To further potentially tailor the nano–bio interface, we encapsulated SFNPs within a lipid shell composed of 1,2-dihexadecanoyl-sn-glycero-3-phosphocholine (DPPC), cholesterol, and 1,2-Dimyristoyl-rac-glycero-3-methoxypolyethylene glycol-2000 (DMG-PEG 2000), produced by microfluidics, and subsequently enriched the membrane with mesenchymal stromal cell-derived extracellular vesicles (EVs). PEGylation was included to reduce protein adsorption and opsonization, potentially improving colloidal stability and circulation behavior.[12,13] EVs' fusion was introduced as a modular strategy to engineer the outer membrane interface of the carrier-in-carrier system, enabling incorporation of native membrane-associated components into an otherwise synthetic lipid shell. In this design, the SFNP core provides the drug-loaded protein matrix, whereas the lipid/EV shell acts as an engineerable external interface that can reduce aggregation, modulate release, and provide a biomimetic membrane environment without requiring covalent modification of the protein carrier. The aim of adding EVs is to tune membrane composition/organization and, consequently, the interfacial signatures of the hybrid nanosystems. The "hybridization" of synthetic lipids with EVs shell is intended, according to the literature data, to reduce immune recognition (stealth effect) and exploit the natural tropism of EVs toward inflamed tissues.[14] Finally, the nanosystems loaded or unloaded with curcumin were characterized to resolve size, ζ-potential, morphology, and internal structure at the nanoscale, using complementary techniques including small-angle X-ray scattering (SAXS), confocal microscopy, atomic force microscopy (AFM), Fourier Transform Infrared (FTIR) spectroscopy, circular dichroism (CD), and asymmetric flow field-flow fractionation (AF4). Each technique was selected to provide a complementary structural or interfacial readout: ensemble colloidal properties (DLS/zeta-potential), size-resolved structural heterogeneity (AF4-SAXS), nanoscale architecture and shell organization (SAXS modeling), molecular interactions and secondary structure (FTIR/CD), and direct morphological validation (confocal microscopy and AFM). The overall design and sequential formulation strategy are summarized in Figure 1.

The novelty of this work lies in a multilevel approach to design the nanocarrier, enabling precise control of silk conformation and the creation of a biomimetic tunable hybrid interface for drug delivery. This research represents the structure-based proof-of-concept study that confirmed the carrier-in-carrier production feasibility; further studies will be performed to investigate the cellular uptake ability and other biological effects of the promising developed systems.

■ MATERIALS AND METHODS

Materials

Silk fibroin (SF) was extracted from *B. mori* cocoons (Orgosolo strain) and provided by local breeders. Curcumin ($C_{21}H_{20}O_6$, molecular weight 368.38 g/mol, purity >65%) was used as the model drug and was purchased from Merk Life Science S.r.l. (Milan, Italy). The reagents used for fibroin processing and nanoparticle preparation included sodium carbonate anhydrous (Na_2CO_3, molecular weight 105.99 g/mol, purity 99.5%, AnalytiCals, Carlo Erba, Milan, Italy), lithium bromide (LiBr, molecular weight 86.84 g/mol, purity >99%, Merck Life Science S.r.l.), and calcium chloride anhydrous ($CaCl_2$, molecular weight 110.98 g/mol, purity >96%, MerckLife Science S.r.l.), 25-NBD cholesterol (25-[*N*-[(7-nitro-2-1,3-benzoxadiazol-4-yl)methyl]amino]-27-norcholesterol), DPPC (1,2-dihexadecanoyl-sn-glycero-3-phosphocholine) and DMG-PEG2000 (1,2-Dimyristoyl-rac-glycero-3-methoxypolyethylene glycol-2000) were purchased from Avanti Polar Lipids inc. (Alabaster, AL, USA) while cholesterol was from Merck Life Science S.r.l.. Ethanol and acetone were both supplied by Carlo Erba.

Degumming of *B. mori* Cocoons and SF Solubilization

To remove sericin and obtain pure fibroin for subsequent applications, a degumming process using sodium carbonate (Na_2CO_3) was employed. As previously reported,[15,16] *B. mori* cocoons were cut into small pieces and rinsed with water to remove surface impurities. Then the cocoons were immersed in 0.2 M sodium carbonate aqueous solution, heated, and maintained at 100 °C (1 g of cocoons in 400 mL of solution). Following the degumming procedure, the fibroin was rinsed with 60 °C water to remove residual salts and any sericin residues trapped within the fibroin fibers.[15] After the final washing step, the purified fibroin was manually compressed to eliminate excess water and subsequently air-dried to obtain a fully purified fibroin. After that, fibroin was dissolved in 9.3 M LiBr (fibroin concentration 25% w/v) at different temperatures and time conditions that were selected from the literature:[17] 25 °C for 6 h (SFNPs-25) and 60 °C for 4 h (SFNPs-60). Subsequently, the SF solutions were dialyzed using a 3.5 kDa molecular weight cut-off (MWCO) cellulose membrane (Spectrum Laboratories, Milan, Italy) to remove any traces of solvent, yielding a water solution

Downloaded from pubs.acs.org/aamick/article-pdf/doi/10.1021/acsami.6c16066/6193937/am-2026-160662.pdf by guest on 15 November 2026

https://doi.org/10.1021/acsami.6c16066
ACS Appl. Mater. Interfaces XXXX, XXX, XXX–XXX

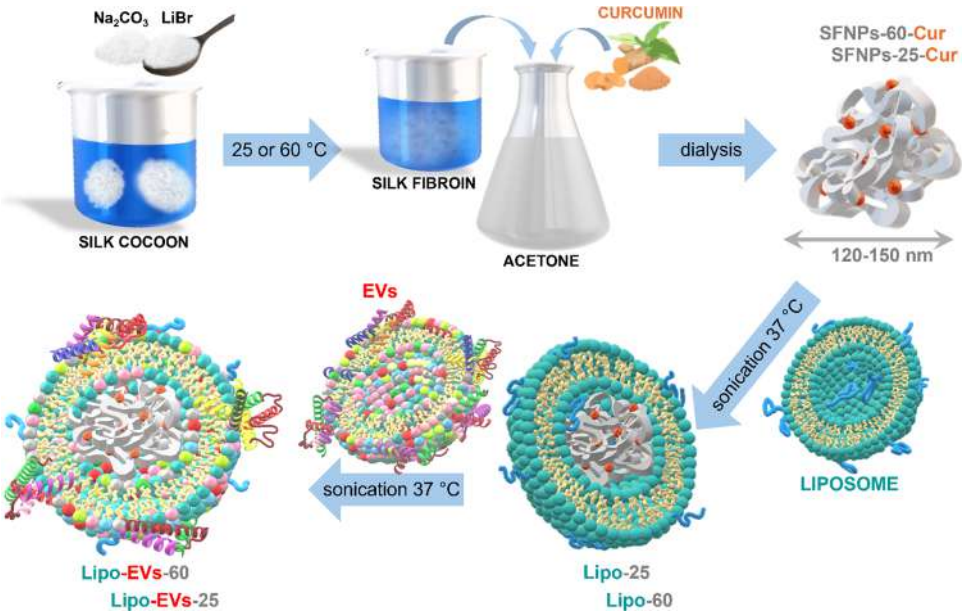


Figure 1. Carrier-in-carrier formulation: degumming of *B. mori* cocoons using Na_2CO_3, SF solubilization with LiBr at 25 or 60 °C, desolvation in acetone with curcumin to prepare SFNPs with encapsulated curcumin (SFNPs-25-Cur and SFNPs-60-Cur), sonication of SFNPs-Cur mixed with liposomes to load the SFNPs into liposomes (Lipo-25 and Lipo-60), and fusion with EVs (Lipo-EVs-25 and Lipo-EVs-60). The schematic summarizes the key findings of this study, including successful curcumin encapsulation and SFNPs loading into liposomes, preservation of the lipid bilayer structure in the outer shell of the carrier-in-carrier system, and incorporation of EV-associated proteins into the lipid shell.

suitable for SFNPs preparation. Then they were stored at 40 °C and proved stable for at least 1 month.

Silk Fibroin Nanoparticle Preparation

SFNPs were produced using a desolvation method, employing acetone as the desolvating agent, according to a procedure reported in the literature.[18–20] Diluted SF solution (3% w/v) was added dropwise into acetone or curcumin solution in acetone at different concentrations, maintained under gentle stirring (Table 1). Obtained NP suspensions were then subjected to dialysis using a 14 kDa MWCO cellulose membrane to remove residual solvents and unencapsulated curcumin and obtain an aqueous suspension of SFNPs. The suspensions were frozen and lyophilized using an Epsilon 2–4 LSCplus Pilot Freeze Dryer (Martin Christ, Germany) through a multi-stage lyophilization process: a primary drying to sublimate frozen water (8×10^{-2} mbar, −25 °C), and secondary drying to remove residual bound water (8×10^{-2} mbar, −5 °C). This protocol ensured the production of dried SFNPs powder, suitable for storage at room temperature (r.t., 25 °C) and further characterizations. For each considered formulation (Table 1), at least three batches were produced and analyzed. Formulation (A) corresponds to a low initial curcumin concentration (0.1 mg/mL) and formulation (B) to a high initial curcumin concentration (0.5 mg/mL).

Liposome Preparation

Two liposome formulations, with and without fluorescent cholesterol, were prepared using a microfluidic system (Dolomite instrument) equipped with a 5-input microfluidic chip. The lipid phase was prepared by dissolving lipid components in ethanol at a final concentration of 5 mg/mL, specifically for non-fluorescent liposomes (Lipo) DPPC:Cholesterol:DMG-PEG2000 at a molar ratio of 64:33:3, while for fluorescent liposomes (LipoNDB) DPPC:Cholesterol:DMG-PEG2000:25-NDB cholesterol at a molar ratio of 64:32.67:3:0.33. Lipid solutions and water, selected as the aqueous phase, were filtered using a syringe filter with a pore size of 0.22 μm before use. The flow rate ratio (FRR) between the lipid and aqueous phases was set at 3:1, while the total flow rate (TFR) was fixed at 2000 μL/min. The obtained liposome suspensions were dialyzed against water to remove residual ethanol. Samples were stored at 4 °C until use.

Extracellular Vesicles Preparation

Extracellular vesicles (EVs) were isolated and purified from adipose-derived mesenchymal stromal cells (MSCs) using a procedure previously published.[21,22] Briefly, MSCs were cultured until sub-confluence, and the secretome release was induced by serum deprivation. The conditioned media were collected, purified, and concentrated by tangential flow filtration (KrosFlo® Research 2i system, Spectrum Laboratories,

Table 1. Preparation Conditions for SFNPs: Degumming Temperature and Time, and Curcumin Concentration in the Acetone Bath[a]

formulations	temperature of solubilization (°C)	time of solubilization (h)	curcumin concentration (mg/mL)
SFNPs-60	60	4	/
SFNPs-25	25	6	/
SFNPs-60-Cur(A)	60	4	0.1
SFNPs-25-Cur(A)	25	6	0.1
SFNPs-60-Cur(B)	60	4	0.5
SFNPs-25-Cur(B)	25	6	0.5

[a]All fibroin used for this study was degummed with lithium bromide.

https://doi.org/10.1021/acsami.6c16066
ACS Appl. Mater. Interfaces XXXX, XXX, XXX−XXX

Downloaded from pubs.acs.org/aamick/article-pdf/doi/10.1021/acsami.6c16066/69193937/am-2026-160662.pdf by guest on 15 November 2026

Milan, Italy). EVs were retained using a 300 kDa MWCO filtration module (Spectrum Laboratories). Obtained EVs suspension was lyophilized (8×10^{-1} mbar and –50 °C for 72 h, instrument Christ Epsilon 2–16D LSCplus) using mannitol (0.5% w/v) as cryoprotectant. The powder was preserved at –20 °C until use.

Carrier-in-Carrier System Preparation

Different carrier-in-carrier hybrid system formulations were prepared considering the following variables: SFNP formulation (with higher curcumin content: formulation B), liposome formulation, and presence/absence of extracellular vesicles (Table 2). The addition of EVs to liposomes was intended to promote hybridization of the synthetic liposomal membrane with EV-derived membrane components. The encapsulation of SFNPs in the liposome/EV shell was performed using a probe sonicator.[13] The dialyzed liposome suspensions were diluted 1:5 volume ratio, and SFNPs were suspended in water at a final concentration of 3 mg/mL and maintained in a bath sonicator for 20 min. Both suspensions were then filtered through 0.45 μm syringe filters. After that, liposome and SFNP suspensions were mixed (1:1 volume ratio) and ultrasonicated to promote the effective loading of SFNPs into the liposomal shell with a Fisherbrand Ultrasonic Liquid Processor (model FB-505, output frequency of 20 kHz) using 20% amplitude, performing 6 cycles 10 s on/off with 3 min of duration and 2 min of cooling period between each cycle. Subsequently, the obtained mixture was incubated at 37 °C for 1 h.[13] This protocol was applied to all formulations not containing extracellular vesicles (EVs).

For the formulations involving EVs, a modified approach was used: 5 mg of lyophilized EVs, previously rehydrated in 500 μL sterile water, were added to the liposome and SFNP suspensions before the incubation step. The resulting mixture, containing both synthetic liposomes and EVs, was then subjected to the same ultrasonication and co-incubation procedure as described above. This strategy aimed to promote the formation of hybrid vesicular systems, incorporating both artificial and biological membrane components.

Characterization of SFNPs, Liposomes, and Carrier-in-Carrier Systems

Particle Size and Zeta Potential Analysis. The mean size and polydispersity index (PDI) of the SFNPs, liposomes, and carrier-in-carrier systems were assessed using Photon Correlation Spectroscopy (PCS) with an N5 Submicron Particle Size Analyzer (Beckman Coulter, Milan, Italy) equipped with a 25 mW Helium-Neon Laser (632.8 nm). PCS measurements were performed at a 90° detection angle for the scattered light and a temperature of 25 °C. Prior to analysis, lyophilized SFNP powders were resuspended in milliQ water (3 mg/mL), sonicated for 30 min with intermittent vortexing, and filtered through a 0.45 μm hydrophilic cellulose acetate membrane filter to ensure sample homogeneity and the removal of aggregates. Liposome suspension was filtered through a 0.45 μm cut-off polyethersulfone (PES) filter to remove any aggregates from the sample and was analyzed after dilution. Carrier-in-carrier systems were analyzed as prepared.

Zeta potential measurements were conducted using a Zetasizer (Malvern Instruments, UK) with an Omega cuvette (DTS1070, Malvern) under the same conditions: a 90° detection angle, a temperature of 25 °C, and a refractive index of 1.330. Each measurement was performed in triplicate ($n = 3$), following the same sample preparation protocol as that used for particle size analysis.

The experimental data were analyzed by a one-way ANOVA, and the statistical differences between treatment groups were determined by Fisher's least significant difference procedure (LSD) (STATGRAPHICS XVII, Statpoint Technologies, Inc., Warrenton, Virginia, USA).

Secondary Structure of Silk Fibroin. Fourier Transform Infrared Spectroscopy (FTIR) measurements were performed to verify curcumin encapsulation and changes in silk fibroin secondary structure upon curcumin encapsulation or loading to liposomes. In the attenuated total reflectance (ATR) configuration, samples are deposited on a solid ATR crystal, through which the IR beam undergoes multiple internal reflections (12 in the present case). Under the experimental conditions employed, the penetration depth value is on the order of a few μm. ATR-FTIR analysis in the mid-IR range (650–4000 cm^{-1}) was carried out using a Spectrum One FTIR spectrophotometer (PerkinElmer, Monza, Italy) equipped with a MIRacle ATR accessory (PIKE Technologies, Madison, Wisconsin, USA). The measurements were conducted with 64 scans at a resolution of 4 cm^{-1}. The sample was positioned onto a Zinc Selenide (ZnSe) ATR crystal to acquire the spectrum in transmittance mode.[23] Fibroin conformation was assessed via FTIR in aqueous solution immediately after solubilization and dialysis (Silk I), after four weeks of storage at 4 °C, and in its native degummed form (Silk II). On the same instrument, all SFNPs formulation powders (both loaded and blank from both solubilization methods) were analyzed to verify curcumin loading inside the nanoparticles and the presence of characteristic peaks of curcumin. Additional ATR-FTIR spectra of SFNPs resuspended in water and formulations with lipid shell in water were collected using an iS50 Nicolet instrument from Thermo Fisher Scientific. ZnSe was used as an ATR crystal, and it was cleaned with water and ethanol before the experiment. Studied samples were deposited onto a ZnSe crystal and dried at 30–35 °C. The spectra were collected with a resolution of 0.4 cm^{-1} and a total of 64 interferograms per spectrum. For all collected spectra, a baseline correction was performed after a background subtraction. Peak deconvolution was performed using Gaussian functions in OriginLab software.

In addition to FTIR, Circular Dichroism (CD) experiments were performed to obtain additional information on silk fibroin structure.

CD measurements were performed using a spectrophotometer Jasco J1100 in quartz cuvettes of 1 mm thickness. The spectra were recorded in the wavelength range of 180–500 nm at temperatures of 25 and 37 °C. The curves were fitted using the BeStSel web platform for secondary structure determination and fold recognition.[24] All fitting curves, details of the fitting model, and fitting parameters are presented in the Supporting Information, Figure S1. Prior to fitting, the measured ellipticity (in mdeg) was converted into molar extinction, Δε, (in $M^{-1}cm^{-1}$) for a 1 mm quartz cuvette, protein concentration 40 μM, and 20 residues per protein molecule. The experimental curve was smoothed by data averaging on a 2 nm window.

Table 2. Composition of the Carrier-in-Carrier Formulations: SFNPs and Liposome Formulations, and the Presence/Absence of EVs

carrier-in-carrier formulations	SFNP formulation	liposome formulation	extracellular vesicles (EVs)
Lipo-EVs-60	SFNPs-60-Cur(B)	Lipo	Yes
Lipo-EVs-25	SFNPs-25-Cur(B)	Lipo	Yes
LipoNBD-EVs-60	SFNPs-60-Cur(B)	LipoNBD	Yes
LipoNBD-EVs-25	SFNPs-25-Cur(B)	LipoNBD	Yes
Lipo-60	SFNPs-60-Cur(B)	Lipo	No
Lipo-25	SFNPs-25-Cur(B)	Lipo	No
LipoNBD-60	SFNPs-60-Cur(B)	LipoNBD	No
LipoNBD-25	SFNPs-25-Cur(B)	LipoNBD	No

https://doi.org/10.1021/acsami.6c16066
ACS Appl. Mater. Interfaces XXXX, XXX, XXX–XXX

Downloaded from pubs.acs.org/aamick/article-pdf/doi/10.1021/acsami.6c16066/6193937/am-2026-160662.pdf by guest on 15 November 2026

Internal Structure of SFNPs and Carrier-in-Carrier Systems. Small-angle X-ray scattering (SAXS) measurements in batch mode were performed to reveal the form factor of SFNPs and their internal structure. All measurements were conducted at 37 °C. SAXS data for SFNPs were collected at ESRF - The European Synchrotron, Grenoble, France, on SAXS beamline ID02 equipped with an Eiger2 4M detector, X-ray energy of 12.23 keV (wavelength of 1.013 Å) to cover a q-range of 0.0057–0.57 $Å^{-1}$, where q is the transferred scattering vector.[25,26] The sample-to-detector distance was 1.5 m. To reduce radiation damage, solutions were pushed through a flow-through capillary during repeated multiple measurements. Data reduction was performed using the beamline workflow in SAXSutilities software;[27] at least 10 frames per sample were acquired for all samples and averaged, after excluding any radiation damage. The raw data from ID02 beamline at ESRF are available at https://doi.esrf.fr/10.15151/ESRF-ES-1837447272 and https://doi.esrf.fr/10.15151/ESRF-ES-1925860640.

SAXS experiments for SFNPs and formulations were performed using the EMBL P12 beamline of the storage ring PETRA III (DESY, Hamburg).[28] 40 μL of sample was loaded into the flow-through capillary using a sample changer at 37 °C. The measurements were performed at a wavelength of 0.124 nm with an exposure time of 0.1 s. The scattered photons were detected using a PILATUS 6 M detector with a sample-to-detector distance of 3 m. The data were reduced using the SASFLOW pipeline.[29] 40 frames were collected and normalized to the transmitted beam for each sample to make corrections for variations in the sample thickness and beam flux. The scattering from water was subtracted to remove the solvent background. The presented scattering profiles are in absolute intensity scale, calibrated using water. SAXS profiles were fitted with the Mass Surface Fractal model[30,31] and Core Multi-shell model[32] using SASview and SASfit software.[33,34]

SAXS data for SFNPs were fitted using Mass Surface Fractal model[30,31] using SASview software.[33] The following equation was used as a form factor:

$$P(q) = \left(1 + \frac{2q^2R_g^2}{3D_m}\right)^{-D_m/2} \left(1 + \frac{2q^2r_g^2}{3(6 - D_s - D_m)}\right)^{(D_s + D_m - 6)/2} \quad (1)$$

where q is the scattering vector, R_g is the gyration radius of the aggregate, r_g is the gyration radius of the primary particle, D_s is the surface fractal dimension, D_m is the mass fractal dimension.

SAXS curves of liposomes and carrier-in-carrier systems were fitted using Core Multi-shell model[32] using SASview software.[33] The following equation was used as a form factor:

$$P(q) = (K(q, R, \eta - \eta_1) + K(q, R + t_1, \eta_1 - \eta_2) + K(q, R + t_1 + t_2, \eta_2 - \eta_3) + K(q, R + t_1 + t_2 + t_3, \eta_3 - \eta_0))^2 \quad (2)$$

$$K(q, R, \Delta\eta) = 4\pi R^3 \Delta\eta \frac{\sin(qR) - qR\cos(qR)}{(qR)^3} \quad (3)$$

where R is the radius of core, t_1, t_2, t_3 are thicknesses of the first, second and third shell; η, η_1, η_2, η_3 and η_0 are SLDs of core, shells, and solvent respectively. To account for dispersity, a Schulz-Zimm distribution of R was included.

Asymmetric Field Flow Fractionation (AF4) with SAXS measurements (AF4-SAXS) experiments were conducted to investigate the structural heterogeneity of SFNPs. The measurements were performed in the inline setup of P12 beamline (EMBL), DESY.[35] The samples were fractionated using a Postnova instrument (PN AF2000 with an autosampler (PN 5300). A standard AF4 channel was equipped with a regenerated cellulose membrane (10 kDa) and a Mylar spacer (with a height of 350 μm). All measurements were performed at 37 °C. The fractionated samples were detected with a UV detector (PN 3211) and a Multiangle Light Scattering (MALS) detector (PN 3621 with green laser, λ = 532 nm; scattering angles, θ, were 28, 44, 60, 76, 90, 124, 140, and 156°). The UV absorbance wavelength was set to 280 and 360 nm. The MALS outlet was directly connected to the SAXS flow capillary using a minimal tubing length with an ID of 250 μm. The injected volume was 10 μL for AF4-MALS measurements and 250 μL for AF4-MALS-SAXS experiments.[36] The separation protocol consisted of a constant crossflow of 0.6 mL/min and detector flow of 0.5 mL/min. The injection phase (focusing step) was 5 min. After each run, sufficient time for rinsing was allowed. Elution time was converted to elution volume using the detector flow rate. MALS data were analyzed using Nova FFF AF2000 software, including baseline subtraction, peak integration, and calculation of gyration radii, R_g, from angular dependencies using Zimm plot, Berry plot, or Sphere model.

AF4-SAXS measurements were performed at the P12 beamline (see above). The eluent was passed through a 1 mm quartz capillary, while SAXS data with 1 s exposure time were recorded on a Pilatus 6 M area detector (Dectris) at a sample-to-detector distance of 3 m and the wavelength λ = 0.124 nm (X-ray energy 10 keV). AF4-SAXS elution profiles were analyzed using CHROMIXS graphical user interface in ATSAS software.[37,38]

Since SFNPs solutions were filtered using a syringe filter (PVDF, 0.45 μm) prior all experiments, SFNPs concentration was estimated with UV-vis spectroscopy measured with NanoDrop One (Thermo Scientific) at a wavelength 280 nm.

Drug Loading and Encapsulation Efficiency Determination. Curcumin loading within the SFNPs was assessed by dissolving 1 mg of nanoparticles from each batch in 2 mL of 96% ethanol and keeping them under mild stirring for 8 h in the dark. The samples were subsequently centrifuged at 4000 rpm for 10 min to separate the supernatant, which was collected and plated in triplicate into 96-well plates. Absorbance measurements were recorded at 425 nm using a Fluostar OMEGA plate reader (BMG Labtech, Germany). The absorbance of the ethanol solution was used as a blank. The curcumin content was calculated from a calibration curve: a stock solution of curcumin at a concentration of 100 μg/mL was prepared by dissolving 1 mg of curcumin in 10 mL of 96% ethanol. From the stock solution, 6 dilutions were prepared ranging from 1.5 μg/mL to 37.5 μg/mL (R^2 = 0.9973, n = 3). The experimental data were analyzed by a one-way ANOVA, and the statistical differences between treatment groups were determined by Fisher's least significant difference procedure (LSD) (STATGRAPHICS XVII, Statpoint Technologies, Inc., Warrenton, Virginia, USA).

Drug Loading (DL) was calculated as:

$$\text{DL}\,\% = \frac{\text{mg of encapsulated curcumin}}{\text{mg of SFNPs}} \times 100 \quad (4)$$

Encapsulation efficiency (EE) was calculated as:

$$\text{EE}\,\% = \frac{\text{mg of encapsulated curcumin}}{\text{mg of curcumin used for SFNPs production}} \times 100 \quad (5)$$

In Vitro Release Profile of Curcumin from SFNPs and Carrier-in-Carrier Systems. The in vitro release of curcumin from SFNPs was assessed using a dialysis-based method, as previously reported.[18,20,39−41] Precisely, SFNPs (SFNPs-60-Cur(A), SFNPs-60-Cur(B), SFNPs-25-Cur(A), SFNPs-25-Cur(B)) were suspended in deionized water (3.3 mg/ml) and transferred into a dialysis tube with a MWCO of 12–14 kDa. The carrier-in-carrier systems (Formulations Lipo-EVs-60, Lipo-EVs-25, Lipo-60, Lipo-25) were added to the dialysis bag, considering the same equivalent

Downloaded from pubs.acs.org/aamick/article-pdf/doi/10.1021/acsami.6c16066/69193937/am-2026-160662.pdf by guest on 15 November 2026

https://doi.org/10.1021/acsami.6c16066
ACS Appl. Mater. Interfaces XXXX, XXX, XXX−XXX

concentration of SFNPs (3.3 mg/ml). The dialysis membrane containing the suspension was subsequently immersed in 40 mL of 50% ethanol solution (v/v) and maintained under constant magnetic stirring in the dark; the selected solvent mixture is a previously established model able to ensure sink conditions for hydrophobic payloads.[18,20,39–41] To monitor the release kinetics of curcumin, 1 mL aliquots were withdrawn from the ethanol/water medium at predetermined time intervals, spanning from 10 min to 48/72 h (for SFNPs and Carrier-in-Carrier systems, respectively). Following each withdrawal, an equal volume of fresh 50% ethanol was replenished to the release medium to maintain a constant volume and ensure sink conditions throughout the experiment. For quantitative analysis, 100 μL of each aliquot was plated in triplicate onto a 96-well plate, and the absorbance of curcumin was measured at 425 nm using a Fluostar OMEGA plate reader. The obtained data were analyzed by a one-way ANOVA, and the statistical differences between formulations were determined by Fisher's least significant difference procedure (LSD) (STATGRAPHICS XVII, Statpoint Technologies, Inc., Warrenton, Virginia, USA).

Imaging of SFNPs and Carrier-in-Carrier Systems: Curcumin Colocalization and Localization of SFNPs within Liposomes. SFNPs-60-Cur(B), LipoNBD, and LipoNBD-LiBr60 carrier-in-carrier hybrid systems were characterized in terms of morphology and ultrastructure by Transmission Electron Microscopy (TEM) (JEOL JEM-1200EX-II, Milan, Italy). A copper grid (300 mesh) was placed for 1 min on a droplet of each sample. Subsequently, the grids were placed on 2% uranyl acetate solution for 2 min to stain the samples. The excess suspensions were eliminated on filter paper.Confocal microscopy (Leica TCS SP8 STED 3X system) analyses were performed to evaluate and demonstrate the curcumin encapsulation into the SFNPs and the effective encapsulation of SFNPs into the lipid shell. 10 μL of SFNPs-60-Cur(B) or 10 μL of LipoNBD-60 suspension were placed on a glass slide and covered with a coverslip. Each sample was examined under different excitation wavelengths, λ_{ex}, and emission wavelengths, λ_{em}, specifically selected and optimized to detect the individual components of SFNPs and carrier-in-carrier system: λ_{ex} 405 nm, λ_{em} 420–480 nm for curcumin, λ_{ex} 488 nm, λ_{em} 500–600 nm for SF, and λ_{ex} 543 nm, λ_{em} 565–575 nm for 25-NBD cholesterol. The pinhole was set to 286.5 microns to optimize image acquisition and ensure a balance between resolution and signal intensity.

Images of unloaded SFNPs and curcumin-loaded SFNPs were acquired to confirm the co-localization of the active compound within the silk fibroin structure. Following this, liposomes alone were analyzed to optimize the filter settings and define the best experimental conditions for imaging. Finally, the carrier-in-carrier hybrid system was examined by acquiring two separate images using filters specific for curcumin and 25-NBD cholesterol used for liposome preparation. These images were subsequently overlaid to assess the spatial distribution and potential co-localization between the two components, providing further insight into the structural organization of the system and the successful encapsulation of loaded-SFNPs inside liposomes.

Atomic Force Microscopy (AFM) was measured for a carrier-in-carrier system in a liquid cell using the Oxford Instruments Cypher VRS1250 (Asylum Research) microscope and silicon AFM probe Olympus BL-AC40TS-C2 with resonant frequency 110 kHz (resonant frequency in water 25 kHz, spring constant 0.09 N/m). For experiment, freshly cleaved mica was treated with 0.01 mg/ml poly-L-lysine or 10 mM $CaCl_2$ solution for 15 min at room temperature to screen the surface charge of mica, washed with water to remove the excess of poly-L-lysine or $CaCl_2$ and then the solution with formulation in water (10 mg/mL, 80 μL) was deposited onto mica and equilibrated for 20 min at 37 °C. All measurements were performed in the AC liquid imaging mode at 37 °C. Images were acquired at a scan rate of 1.45 Hz with 512 × 512 points and lines. The background subtraction and cross-section analysis for AFM images were performed using Gwyddion software.[42]

Therefore, each characterization technique was selected to provide a complementary structural or interfacial readout: ensemble colloidal properties (DLS/ζ-potential), size-resolved structural heterogeneity (AF4-MALS-SAXS), nanoscale architecture and shell organization (SAXS modeling), molecular interactions and secondary structure (FTIR/CD), and direct morphological validation (confocal microscopy and AFM).

RESULTS AND DISCUSSION

Secondary Structure of Silk Fibroin within SFNPs

Since the secondary structure of silk fibroin plays an important role in nanoparticle properties and is affected during nanoparticle preparation, we employed FTIR spectroscopy to investigate its native degummed form (Silk II), freshly prepared aqueous solutions (Silk I), and solutions stored at 4 °C for 28 days. Native silk fibroin fibers, subjected to degumming with sodium carbonate, exhibited characteristic FTIR peaks indicative of a high β-sheet content, confirming their stable Silk II conformation (Figure 1). Specifically, bands at 3281 cm^{-1} (N–H stretching of the primary amide), 1620 cm^{-1} (C–O stretching of the primary amide), 1512 cm^{-1} (N–H bending), and 1403 cm^{-1} (C–N bending) were observed, all of which being associated with the ordered and rigid structure of β-sheets (Figure 2). In contrast, fibroin solutions in the Silk I state displayed a different spectral profile, with the primary amide C–O stretching peak shifted to a higher wavenumber (1638 cm^{-1}), accompanied by an N–H stretching peak at 3296 cm^{-1} and an N–H bending peak at 1542 cm^{-1}. The absence of the C–N bending peak, typically associated with solid-state fibroin, further confirmed the presence of Silk I, a less structured and more hydrated conformation. Over time, Silk I fibroin undergoes a progressive conformational shift towards Silk II. This transition is marked by a gradual reorganization of polypeptide chains into β-sheet structures, leading to increased viscosity and a denser molecular arrangement. FTIR spectra of fibroin stored at 4 °C (transition fibroin) for four weeks revealed peaks closely resembling those of Silk II, confirming a progressive structural shift towards a more ordered and aggregated conformation. This transition is also associated with an increase in solution viscosity, which ultimately limits the stability and usability of solubilized fibroin. Understanding these conformational dynamics is crucial for optimizing fibroin processing and ensuring its stability for intended applications.

Using FTIR, we were able to evaluate the effect of silk fibroin precipitation as SFNPs on the protein structure as well as curcumin loading within the nanoparticles. The comparison between the spectra of loaded (SFNPs-60-Cur(B) formulation) (Figure S2 and Table 1) and unloaded (SFNPs-60) SFNPs nanoparticles, as well as the difference spectrum (Figure S3) revealed the presence of characteristic peaks of curcumin at 1029 cm^{-1}, corresponding to C–O stretching coupled with adjacent C–C stretching, and at 1125 cm^{-1}, attributed to asymmetric C–O stretching (Figure S2). However, due to the overlapping signals from fibroin and the relatively low drug loading of curcumin within the SFNPs (1.42%), additional curcumin-specific peaks were not distinctly visible. However, a comparative analysis between the spectrum of pure curcumin and the differential spectrum of the loaded and unloaded nanoparticles (Figure S3) allowed us to make a more accurate assessment of drug encapsulation and interaction with the fibroin matrix. The FTIR spectral analysis revealed

Downloaded from pubs.acs.org/aamick/article-pdf/doi/10.1021/acsami.6c16066/6193937/am-2026-160662.pdf by guest on 15 November 2026

https://doi.org/10.1021/acsami.6c16066
ACS Appl. Mater. Interfaces XXXX, XXX, XXX–XXX

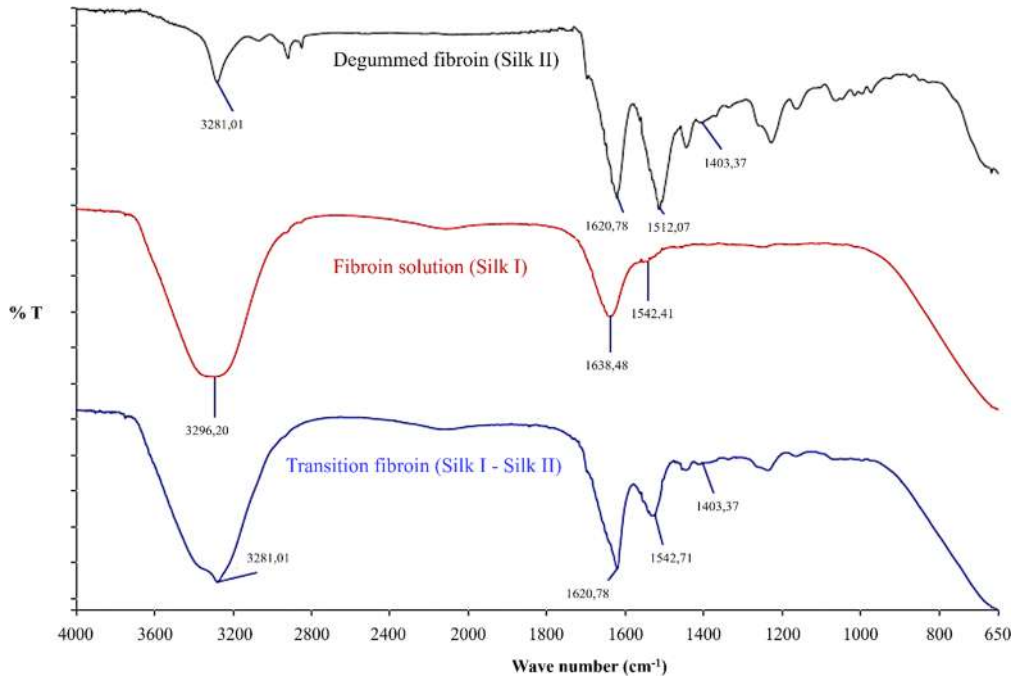


Figure 2. FTIR spectra of silk fibroin (solubilized at 60 °C) aqueous solution immediately after solubilization and dialysis (Silk I), after four weeks of storage at 4 °C (Silk I–Silk II), and in its native degummed form (Silk II).

several distinct characteristic peaks of curcumin, confirming its successful incorporation within the curcumin-loaded SFNPs. Notably, absorption bands were observed at 961 cm^{-1}, corresponding to C–H vibrations of the aromatic ring, and at 1026 cm^{-1}, attributed to C–O stretching coupled with adjacent C–C stretching. Additionally, the spectrum displayed a peak at 1279 cm^{-1}, indicative of C–O–C stretching of the methoxy group, along with a signal at 1456 cm^{-1}, associated with asymmetric CH_3 deformation. Further confirmation of curcumin's presence was provided by absorbance at 1507 cm^{-1}, corresponding to benzene ring stretching. The signal at 1628 cm^{-1} should be interpreted as an overlapping contribution from curcumin C–O stretching and the fibroin Amide I region associated with β-sheet-rich structures. The detection of these characteristic absorption bands in the FTIR spectrum supports the effective encapsulation of curcumin within the SFNPs, highlighting its presence within the fibroin matrix, and a possible curcumin-induced rearrangement of the fibroin secondary structure.

In addition, CD spectroscopy revealed the distortion of the silk fibroin structure by curcumin encapsulation (Figure S1). The CD spectra of unloaded SFNPs-60 have an ellipticity maximum at the wavelength, λ, of 198 m, and a minimum at λ 221 nm. Curcumin loading leads to a shift of the maxima to higher values of λ (202 nm at high drug loading), while the position of the minima is not affected significantly. In order to evaluate the fractions of different secondary structure bases, we fitted the CD spectra using the BeStSel method (Table 3 and Figure S1 and Table S1 in the Supporting Information). The curve fitting shows that the SFNPs consist mainly of β-sheets in antiparallel form (>45%) and other secondary structure bases. Very low content of turns and no helical structures are observed. The loading of curcumin at low concentration (SFNPs-60-Cur(A)) does not affect the ratio of different fractions; however, at higher loading (SFNPs-60-Cur(B)), the fraction of turns undergoes a twofold decrease, and a high fraction

Table 3. Fractions of α-Helices, Parallel and Antiparallel β-Sheets, Turns, and Other Secondary Structure Basis Components Obtained from Fitting CD Spectra Using the BeStSel Method[24]

	fraction, %				
sample	helix	antiparallel	parallel	turn	others
SFNPs-60	0	46.4 ± 0.4	0	10.6 ± 0.2	43.0 ± 0.4
SFNPs-60-Cur(A)	0	44.9 ± 0.4	0	11.4 ± 0.2	43.7 ± 0.4
SFNPs-60-Cur(B)	0	50.4 ± 0.5	20.1 ± 0.3	4.8 ± 0.1	24.7 ± 0.3

of parallel β-sheets is formed, that indicated major rearrangement of protein β-sheets within the nanoparticle due to the incorporation of hydrophobic drug. These results support the FTIR observation of a band at 1628 cm^{-1}, characteristic of β-sheet-rich structures, and confirm that curcumin induces rearrangement of the secondary structure of fibroin. It is worth noting that curcumin is an achiral molecule that absorbs primarily in the 300–500 nm range and does not exhibit intrinsic circular dichroism (CD) in its free form; therefore, its direct contribution to protein secondary structure analysis in the far-UV region (190–240 nm) is expected to be limited. In addition, the comparison of FTIR spectra for SFNPs-25 and SFNPs-60 (Figure S1 in the Supporting Information) showed significantly higher content of β-sheets structures for SFNPs prepared at 60 °C and, thus, more efficient protein unfolding.

Using a combination of FTIR and CD spectroscopy, changes in the secondary structure of silk fibroin were observed following curcumin encapsulation. In particular, the encapsulation of the hydrophobic drug increased the relative fraction of β-sheet structures. This conformational compaction of silk fibroin may potentially affect the organization of the protein within the nanoparticles and, consequently, their surface properties.

Downloaded from pubs.acs.org/aamick/article-pdf/doi/10.1021/acsami.6c16066/6193937/am-2026-160662.pdf by guest on 15 November 2026

https://doi.org/10.1021/acsami.6c16066
ACS Appl. Mater. Interfaces XXXX, XXX, XXX–XXX

Drug Loading and Encapsulation Efficiency

The curcumin encapsulation in SFNPs at 2 starting concentrations (0.1 and 0.5 mg/mL) was tested to determine drug loading (DL %) and encapsulation efficiency (EE %) of the SFNPs (Table 4). SFNPs prepared at a lower initial concentration of curcumin (SFNPs-25-Cur(A) and SFNPs-60-Cur(A)) exhibit significantly lower (around 1%) (One-way ANOVA, $p < 0.05$) DL values with respect to the formulation prepared at 5 times higher curcumin concentration (SFNPs-25-Cur(B) and SFNPs-60-Cur(B)), independently of the fibroin solubilization temperatures (25 or 60 °C). Using the higher selected curcumin concentration (B), a significant (One-way ANOVA, $p < 0.05$) DL increase was observed: SFNs-60-Cur(B) formulation reached 6.4 ± 0.9%, and SFNs-25-Cur(B) achieved DL at 5.9 ± 1.6%. Encapsulation efficiency ranges from 76 to 85%, without any significant differences ($p > 0.05$) between the treatment groups. These findings indicate that the curcumin concentrations used during SFNP preparation strongly influence the drug loading but not the encapsulation efficiency. Therefore, the high drug loading can be achieved by varying the initial curcumin concentration, as previously demonstrated.[18]

Further confirmation of curcumin loading into SFNPs comes from confocal microscopy measurements. We analyzed SFNPs-60-Cur(B) suspension using specific excitation/emission filters for curcumin and fibroin (Figure 3). The images corresponding to the individual signals of curcumin and fibroin are presented in color scale to enhance visibility of single components: red was used for the fibroin signal, while magenta was used for curcumin to differentiate their distribution clearly. In the merged image, the co-localization of curcumin and fibroin results in a red-purple signal, which emerges from the combination of the two fluorescence emissions. These findings reinforce evidence for an effective encapsulation of curcumin within SFNPs. Our results confirmed that this instrumental approach resulted in a good strategy to demonstrate the co-localization of nanoparticles and their cargo,[43] but also opens the possibility to follow and localize the nanosystems into cell compartments during future in vitro experiments.

Thus, drug loading and confocal microscopy imaging demonstrated the colocalization of curcumin with SFNPs. The encapsulation efficiency was found to be independent of the curcumin concentration but dependent on the SFNPs preparation method. In particular, higher encapsulation efficiency was observed for SFNPs prepared at 60 °C, which may be associated with their higher β-sheet content, resulting in increased conformational stability and compactness of the silk fibroin matrix. The formation

Table 4. Drug Loading (DL %) and Encapsulation Efficiency (EE %) Results[a,b]

formulations	DL %	EE %
SFNPs-60-Cur(A)	1.38 ± 0.06*	85 ± 4
SFNPs-60-Cur(B)	6.40 ± 0.90§	83 ± 12
SFNPs-25-Cur(A)	1.30 ± 0.03*	79 ± 2
SFNPs-25-Cur(B)	6.00 ± 2.00§	76 ± 16

[a]Data are expressed as mean values and standard deviations ($n = 3$). [b]Different symbols indicate statistical differences between treatment groups ($p < 0.05$), no symbols mean no significant differences ($p > 0.05$) (One-way ANOVA).

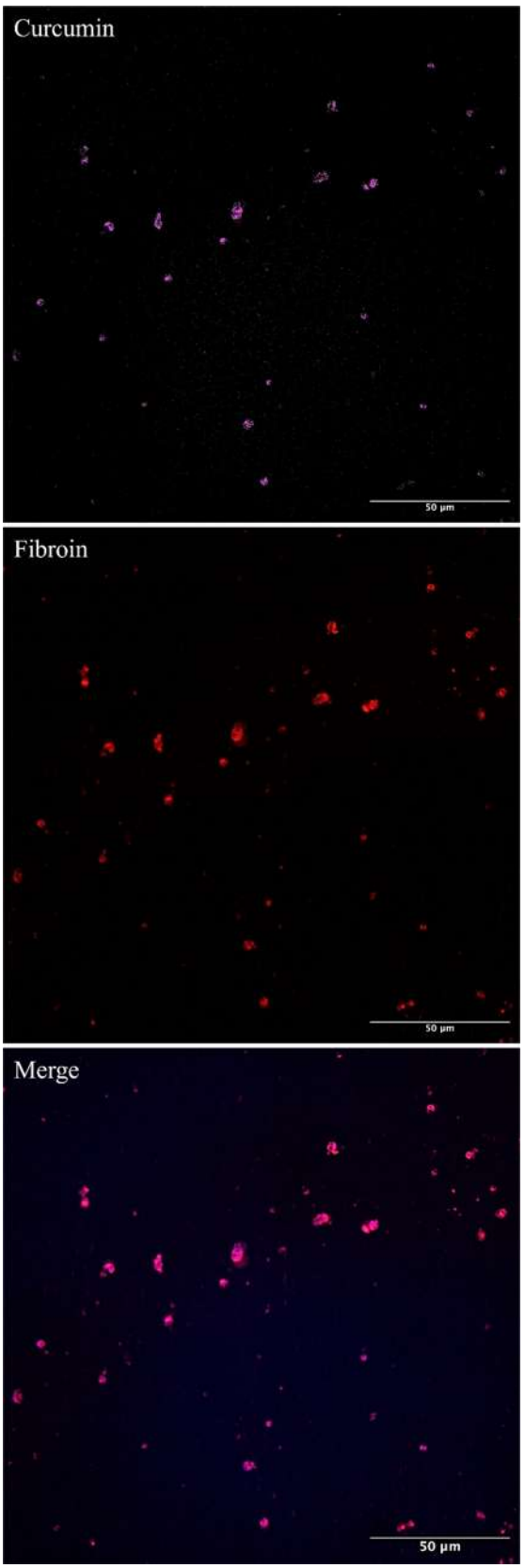


Figure 3. Confocal microscopy images of SFNPs-60-Cur(B) suspension obtained using different excitation/emission channels (specific for each SFNPs component): curcumin (λ_{ex} 405 nm, λ_{em} 420–480 nm), fibroin (λ_{ex} 488 nm, λ_{em} 500–600 nm), and merged image of the two channels (magenta and red for curcumin and fibroin, respectively).

Downloaded from pubs.acs.org/aamick/article-pdf/doi/10.1021/acsami.6c16066/69193937/am-2026-160662.pdf by guest on 15 November 2026

https://doi.org/10.1021/acsami.6c16066
ACS Appl. Mater. Interfaces XXXX, XXX, XXX–XXX

of β-sheet-rich domains may promote intermolecular interactions and reduce protein-chain mobility, thereby favoring the retention of hydrophobic curcumin within the nanoparticle.

SFNPs Size and Morphology: Effect of Curcumin Encapsulation

Efficient drug delivery critically depends on the interfacial properties of the carrier, which can be rationally modulated through control of nanoparticle size, morphology, and surface charge. These parameters govern key biological interactions, including colloidal stability, cellular uptake, and drug–carrier interactions. Accordingly, the size and ζ-potential of SFNPs were determined by light scattering techniques. All tested formulations exhibited mean hydrodynamic diameters ranging from approximately 120 to 150 nm, with no statistically significant differences observed between the groups (Figure 4). However, clear differences emerged between data obtained through intensity-based and number-based size distributions. The intensity-weighted values of mean hydrodynamic diameter (green bars, 125–150 nm) are consistently higher than the number-weighted ones (blue bars) due to the stronger scattering from larger particles (comparable with the wavelength of incident light). The polydispersity index (PDI), indicated by red dots (Figure 4), generally ranged between 0.1 and 0.3 across all samples, suggesting a moderate size heterogeneity, probably due to the aggregation of lyophilized SFNPs. Such variability falls within acceptable limits for stable colloidal systems, indicating good control over the formulation process. Transmission Electron Microscopy (TEM) of the same formulations revealed the presence of big aggregates but also allowed for the identification of individual SFNPs with markedly smaller diameters (Figure S4), indicating that the actual size of the primary nanoparticles is likely lower.

The ζ-potential analysis reveals that fibroin solubilization conditions and curcumin loading did not influence the surface charge of SFNPs (Table 5). All nanoparticles presented a negative ζ-potential variable from –23 to –28 mV, which increases the stability of SFNPs due to the electrostatic repulsion.

Freeze-dried SFNPs remained stable, in terms of size, PDI, and zeta potential, for at least one year when preserved at room temperature and protected from light (data not shown).

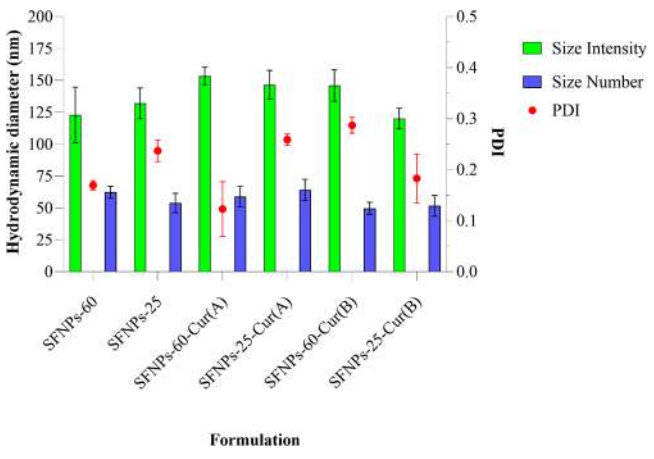


Figure 4. Hydrodynamic diameter (intensity- and number-weighted) and PDI of the investigated SFNPs obtained from PCS measurements. Data are expressed as mean values and standard deviations obtained by analyzing at least two batches for each considered formulation.

Table 5. SFNPs ζ-Potential[a]

SFNPs formulations	ζ-potential (mV)
SFNPs-60	–28 ± 1.0
SFNPs-25	–26 ± 2.0
SFNPs-60-Cur(A)	–28 ± 0.9
SFNPs-25-Cur(A)	–24 ± 1.4
SFNPs-60-Cur(B)	–27 ± 3.0
SFNPs-25-Cur(B)	–26 ± 1.2

[a]Data are obtained from two batches for each considered formulation.

Considering the heterogeneity of the size distribution in the samples, we implemented a fractionation method to investigate the sizes and morphology of the diverse SFNPs sub-families. Asymmetric Field Flow Field Fractionation (AF4) combined with Multiangle Light Scattering (MALS), UV-vis, and small-angle X-ray scattering (SAXS) enabled us to separate fractions by size and permit detailed structural characterization of the predominant SFNP subpopulation (Figure 4a–d). SAXS curves represent the intensity of X-rays scattered at different scattering vectors, q, which are related to distances, d, in real space according to $d = 2\pi/q$ and can be used to extract information about the structural properties of the nanoparticles across different nanometric length scales. Figure 4a,c show the elution profiles, i.e., the signal intensity on the detectors (MALS, UV-vis, SAXS) as a function of elution volume, V. UV-vis and MALS measurements show 2 distinct elution peaks in the AF4 fractogram, suggesting 2 separate particle populations or size fractions for both loaded and unloaded formulations. The corresponding SAXS elution profiles (Figure 4a,c, green traces) exhibit partial overlap, suggesting reduced fractionation resolution due to band broadening and the lower signal-to-noise ratio at low particle concentrations. Nevertheless, analysis of the first-eluting frames allowed us to extract structural information on the SFNPs without interference from larger particles.

The mean gyration radius, R_g, for each fraction was calculated using the Zimm plot, Berry or Sphere model from the angular dependences of scattering intensity (Figure S5 in the Supporting Information). The mean R_g of unloaded SFNPs for the first fraction was found to be 114 ± 2 nm for both SFNPs-25 and SFNPs-60, while the second fraction consists of larger particles with R_g above 140 nm and a broader size distribution (Figure 5 and Figure S5 in the Supporting Information). Molar masses of the SFNPs were also estimated by AF4 (Figure S5 in the Supporting Information), and the elution profiles showed that the first peak corresponds to much lower molar mass NPs (1,000–2,000 kg/mol) in comparison to the second peak (8,000–23,000 kg/mol). The encapsulation of curcumin does not affect the positions of elution maxima but affects R_g values calculated from MALS. For SFNPs prepared at 25 °C (SFNPs-25-Cur(B), Figure S5 in the Supporting Information), the mean values of R_g for both fractions decrease significantly to 90 and 98 nm, indicating formation of more compact aggregates due to the hydrophobic interaction between curcumin and silk fibroin that triggers more compact arrangement of the protein within nanoparticles. For SFNPs prepared at 60 °C the mean sizes are barely affected and slight increase in R_g of larger fraction can be interpreted as a trend, given the broad distribution and lower relative abundance of this population. This behavior may be explained by the higher β-sheet content of SFNPs prepared at higher temperatures, which contributes to a more rigid protein network,

Downloaded from pubs.acs.org/aamick/article-pdf/doi/10.1021/acsami.6c16066/6193937/am-2026-160662.pdf by guest on 15 November 2026

https://doi.org/10.1021/acsami.6c16066
ACS Appl. Mater. Interfaces XXXX, XXX, XXX–XXX

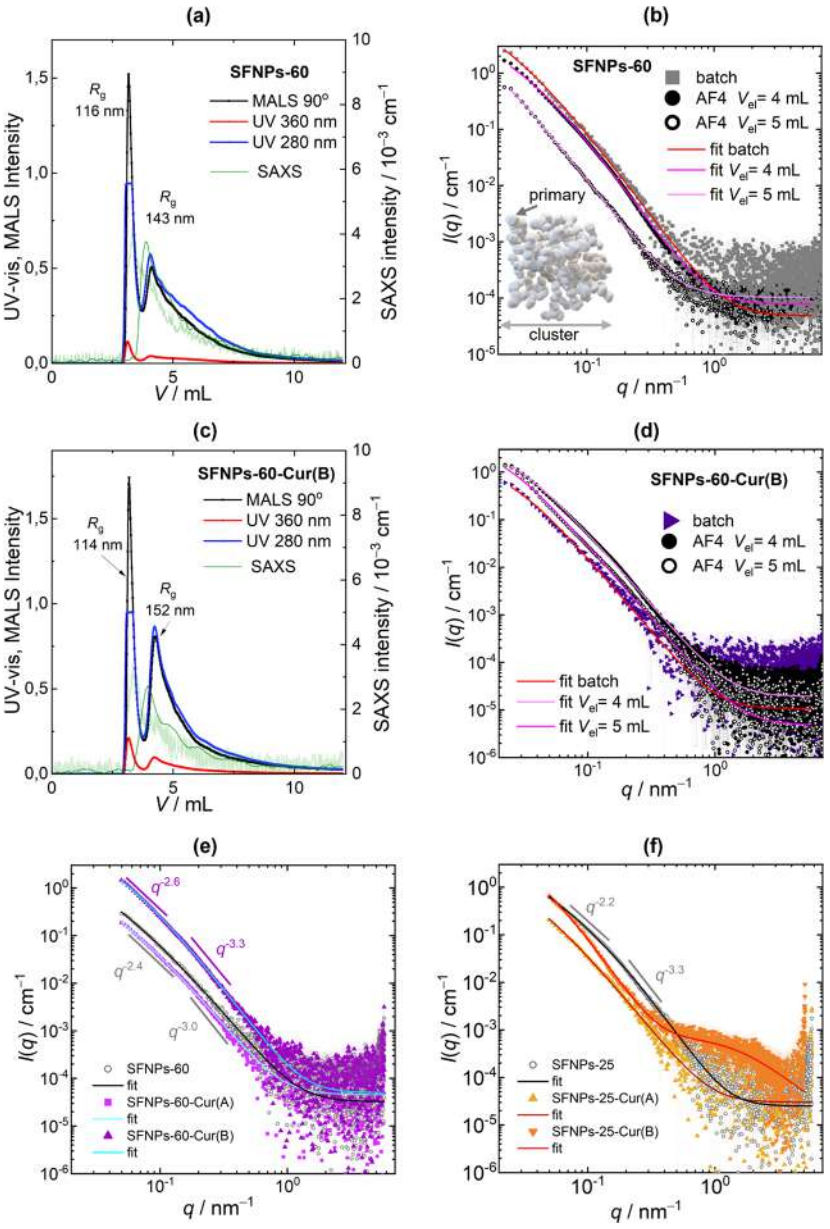


Figure 5. AF4-MALS-UV and AF4-SAXS elution profiles for (a) SFNPs without curcumin (SFNPs-60) and (c) with loaded curcumin (SFNPs-60-Cur(B)). Light green lines are the experimental SAXS elution profiles and dark green lines are the profiles smoothed using the Savitzky-Golay function. The R_g values were calculated from MALS; the error bars did not exceed 2%. (b, d) SAXS profiles of the SFNPs measured in the batch-mode and after fractionation with AF4 (at the peak position if not indicated otherwise). (e, f) SAXS profiles of NPs with (colored symbols) or without (gray symbols) loaded curcumin measured in water at 37 °C. The lines represent the fitting of the curves using the Mass Surface Fractal model. The SAXS intensity was corrected for NP concentration variation after filtration, estimated from UV–vis absorbance of NPs at a wavelength of 280 nm.

while drug-induced hydrophobic interactions promote interparticle association, leading to the formation of larger aggregates. It is worth noting that the ratio of two fractions is affected by curcumin encapsulation: for SFNPs-25, the relative intensity of the first peak increased almost twice due to the curcumin encapsulation, indicating an increase in the number of smaller aggregates, while for SFNP-60, the fraction of larger aggregates increased 1.4 times. These results suggest that curcumin loading into NPs influences both the equilibrium between the two fractions and the size of the aggregates. Moreover, R_g values calculated from AF4-MALS are significantly higher than R_H values obtained from DLS (ca. 1.5 times), which implies that the nanoparticles are not densely packed spherical particles, but rather loose aggregates of Gaussian chains.

To gain further insight into the internal structure of the nanoparticles, we conducted small angle X-ray scattering (SAXS) experiments for the SFNPs before and after separation with AF4 (Figure 5). Although AF4 with conventional detectors shows two peaks, the AF4–SAXS elution profile only exhibits a single peak, indicating reduced resolution due to band broadening and the overall lower detection sensitivity of SAXS at the applied particle concentrations. Since the intensity of the second peak is significantly lower in comparison to the first one, it might be insufficient to resolve it in SAXS elution profiles.

Downloaded from pubs.acs.org/aamick/article-pdf/doi/10.1021/acsami.6c16066/69193937/am-2026-160662.pdf by guest on 15 November 2026

https://doi.org/10.1021/acsami.6c16066
ACS Appl. Mater. Interfaces XXXX, XXX, XXX–XXX

In Figure 4, SAXS curves of unloaded SFNPs (SFNPs-60, Figure 5b) and with encapsulated curcumin (SFNPs-60-Cur(B), Figure 5d) measured in the batch mode are compared with the ones obtained from AF4-SAXS at different elution volumes. The shape of the curves remains largely unchanged after fractionation, suggesting that the two fractions exhibit no substantial morphology differences, as well as high polydispersity of each fraction and particle stability in the flow. In the mid-q range ($0.1 < q < 0.3$ nm^{-1}), related to structuring on distances of tens of nm in the direct space, SAXS profiles of the NPs show a slope ranging from −3.4 to −3. The slope value is consistent with the self-assembly of silk fibroin into non-densely packed fractal aggregates, which is consistent with our finding from the R_g/R_H ratio. These aggregates are formed by polydisperse amorphous loose particles that do not exhibit any characteristic form factor on the investigated length scale. However, their overall mesostructured and surface properties can differ, and this information can be extracted from SAXS curve modeling.

We compared the SAXS profiles collected from SFNPs with different curcumin loading (0, 1, and 6%) and fitted them using a Mass Surface Fractal model (Figure 5e,f) that models the sample as a loose aggregate composed of smaller primary particles. In this model, the fitting parameters are the mass fractal dimension, D_m, related to mass distribution within clusters, surface fractal dimension, D_s, describing roughness of the clusters' surface, and R_g of the clusters and of primary particles. At higher q values, corresponding to smaller distances in the direct space, the scattering profile follows a power law associated with D_s of the primary particles, while at low q, where spectra are sensitive to the structure on larger distances, it follows a power law related to D_m. Data fits show that the cluster R_g is around 90 nm, which matches the results obtained from MALS, and they consist of smaller particles with R_g ca. 10 nm (Table 6), which is in agreement with silk fibroin mass (ca. 400 kDa) and the literature.[44] The fitting model revealed that SFNPs have a surface fractal dimension ($D_s = 2.3$ for and 2.9 for SFNPs-25 and SFNPs-60, respectively) that is slightly higher than the mass fractal one ($D_m = 2.1$ and 2.3), indicating increased surface roughness. Unloaded SFNPs treated at higher temperature (SFNPs-60) show higher D_m and D_s in comparison to the ones treated at lower temperatures (SFNPs-25), indicating that SFNPs-60 may be attributed to the more efficient transition of silk fibroin transition into more compact β-sheets structure due to the higher processing temperature, as also confirmed by FTIR (Figure S1c in the Supporting Information). Curcumin loading leads to an increase in the SAXS scattering intensity, and steeper slope at low q, consistent with the presence of larger and more compact aggregates in solution. Such behavior is likely driven by the pronounced hydrophobicity of curcumin and the resulting hydrophobic interactions with silk fibroin. The surface fractal dimension decreases after curcumin encapsulation to 2.0 for SFNPs-25-Cur(B) and 2.6 for SFNPs-60-Cur(B), while mass fractal dimension increases to 3.3 for SFNPs-25-Cur(B) and 2.5 for SFNPs-60-Cur(B); this as well confirms that upon curcumin loading, NPs offer a more compact structure with a smoother surface in comparison to unloaded nanoparticles. SAXS curves of SFNPs-25-Cur(B) clearly show the presence of smaller molecules in the solution, possibly corresponding to the silk fibroin chains adsorbed onto the nanoparticles; this was taken into account by adding the Polymer Gaussian Coil model[45−47] ($R_g = 1.1 \pm 0.1$ nm). These residues are probably shorter chains of silk fibroin not attached to the SFNPs, since after fractionation with AF4 they were removed from the solution (Figure 5d).

Therefore, regardless of the preparation method, SFNPs form two populations of aggregates that differ in size but do not exhibit significant differences in morphology. Silk fibroin assembles into the loose aggregates, composed of fibroin chains, with the packing density and surface roughness being influenced by the preparation temperature and curcumin encapsulation. In particular, higher preparation temperatures and greater curcumin content result in more compactly packed NPs. This trend may be related to the β-sheet content and strong hydrophobic interactions with curcumin, which may promote more compact packing of the silk fibroin within SFNPs.

Table 6. SAXS Best Fit Parameters Obtained by Modeling the Data with the Mass Surface Fractal Model[30,31] for SFNPs with and without Encapsulated Curcumin[a]

sample	R_g (cluster) nm	R_g (primary) nm	D_m	D_s
SFNPs-25	90 ± 3	10 ± 1	2.12 ± 0.01	2.25 ± 0.02
SFNPs-25-Cur(A)	82 ± 2	10 ± 3	2.75 ± 0.02	2.66 ± 0.03
SFNPs-25-Cur(B)	92 ± 1	10 ± 1	3.25± 0.01	2.0 ± 0.02
SFNPs-60	103 ± 5	10 ± 3	2.25 ± 0.01	2.88 ± 0.07
SFNPs-60-Cur(A)	96 ± 3	10 ± 1	2.32 ± 0.04	2.81 ± 0.01
SFNPs-60-Cur(B)	82 ± 1	10 ± 1	2.50 ± 0.08	2.57 ± 0.04

[a]Reported uncertainties are fitting errors obtained from the SAXS fit.

In Vitro Curcumin Release Profile from SFNPs

The in vitro drug release profiles for all SFNPs-Cur formulations show remarkably consistent behavior, with no statistically significant differences observed between the groups (Figure 6). All samples exhibit a steady and controlled release of curcumin, reaching approximately 90–100% cumulative release after 48 h.

A slightly slower release trend is visible for the (B) formulations (SFNPs-60-Cur(B) and SFNPs-25-Cur(B)), which are characterized by higher drug loading. This minor deviation, particularly noticeable between 4 and 24 h, suggests that the increased curcumin concentration within the fibroin matrix might slightly promote stronger drug-protein

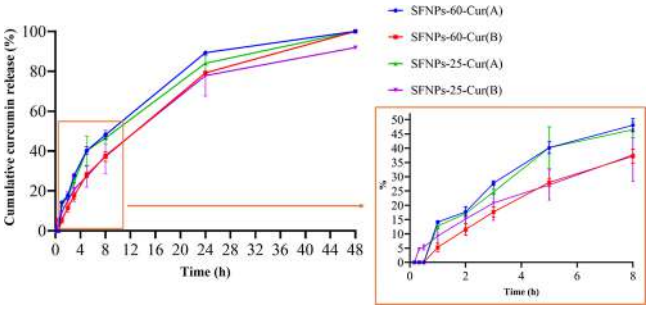


Figure 6. In vitro curcumin release profiles from SFNPs. Data are expressed as mean values and standard deviations obtained by the analysis of at least three independent batches for each considered formulation.

Downloaded from pubs.acs.org/aamick/article-pdf/doi/10.1021/acsami.6c16066/69193937/am-2026-160662.pdf by guest on 15 November 2026

https://doi.org/10.1021/acsami.6c16066
ACS Appl. Mater. Interfaces XXXX, XXX, XXX−XXX

interactions or create a denser hydrophobic core, subtly slowing down diffusion. However, these differences do not alter the overall performance of the delivery system. The initial phase (0–8 h) remains comparable across all groups, with a moderate burst effect likely due to the fraction of curcumin localized in the outer shell of the nanoparticles, as previously suggested by SAXS analysis. Ultimately, the results demonstrate that the silk fibroin carrier provides a reliable and uniform release profile regardless of the specific loading or preparation temperature.

Carrier-in-Carrier System Characterization

In order to improve the stability of the SFNPs and to increase the probability of crossing the cell membrane barrier, SFNPs were loaded into liposomes consisting of cholesterol and phospholipids (DPPC and DMG-PEG2000) intended to create a lipid shell. The SFNPs-25-Cur(B) and SFNPs-60-Cur(B) were loaded into liposomes via sonication and incubated at 37 °C; these formulations were chosen for their higher curcumin content, which allowed us to track the nanosystems also in vitro. Liposomes exhibited an average hydrodynamic diameter (measured by DLS, Figure 7) of approximately 240 nm (PDI 0.102 ± 0.05) for intensity-weighted analysis and 180 nm for the number-weighted analysis with a moderate PDI (0.112 ± 0.01). On the other hand, SFNs-Cur-25(B) displayed a hydrodynamic diameter of approximately 120 nm and 60 nm for intensity and number-based, respectively, before the encapsulation process; this discrepancy between the two values is confirmed by the PDI value of about 0.2. The higher dimensions of liposomes could allow us to generate the lipid shell around the SFNPs structure. The carrier-in-carrier system (formulation Lipo-25) exhibits a slightly reduced average size in intensity-weighted distribution (205 ± 2 nm and PDI 0.25 ± 0.01) compared to liposomes alone; this reduction may be attributed to partial disruption of the liposomal structure during the encapsulation process, followed by reassembly of lipid components around the SFNPs, potentially forming smaller or more compact hybrid systems. Moreover, a positive interaction might occur between lipids and the fibroin core, driving the formation of a more compact system upon mixing. When analyzed in terms of number-weighted distribution, the system shows an even smaller average size, likely to be attributable to

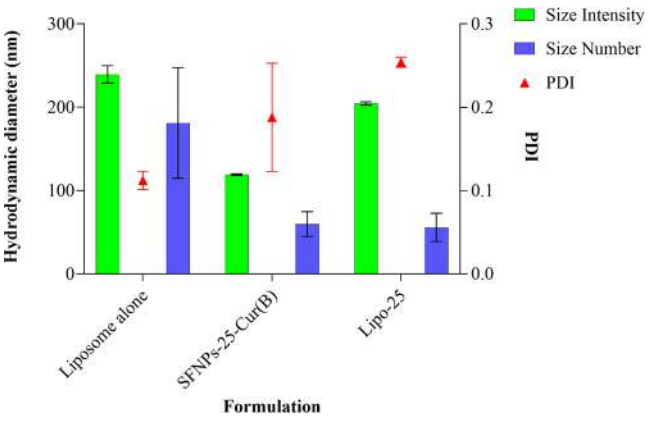


Figure 7. Dimensional characterization of liposomes alone, SFNPs-25-Cur(B), and carrier-in-carrier systems Lipo-25 obtained from PSC measurements. Data has been treated as weighted by intensity or number. Mean values of hydrodynamic diameters and PDI obtained by analyzing at least two batches for each considered formulation are reported.

the presence of individual SFNs freely suspended within the dispersion alongside the liposomes. This bimodal population, comprising both larger liposomes and smaller SFNPs, is characterized by an increase in PDI. No size differences were found between carrier-in-carrier systems obtained with nanoparticle formulations SFNPs-25-Cur (B) and SFNPs-60-Cur(B) (data not shown).

After sonication, the average particle size of the Lipo-25 system (ca. 200 nm) observed in TEM images (Figure S4) suggests partial disruption and reassembly of liposomal membranes during sonication, potentially leading to SFNPs incorporation. While SFNs were clearly observed in the vicinity of liposomes, it remained challenging to ascertain their exact spatial localization, whether internalized within the liposomal core or merely adsorbed onto the surface.

The need to dry the samples to perform TEM can lead to a distorted shape of liposomes or trigger SFNPs release. Therefore, we also visualized the formulation using atomic force microscopy (AFM) in a liquid environment by adsorbing particles onto the mica surface (Figure 8). The images for both samples clearly show the presence of low-height, laterally extended regions, corresponding to liposomal patches. Upon deposition on mica, liposomes partially ruptured and spread into thin and relatively flat supported membrane patches, allowing the membrane thickness to be estimated from AFM cross-section profiles. The polydisperse lateral size of 20–200 nm matches the sizes of liposomes, while the height of approximately 4.5–5 nm is consistent with the thickness of supporting lipid bilayer (statistical analysis of AFM images is presented in Figure S6 in the Supporting Information). The brighter protrusions correspond to SFNPs, which display heights of 20–50 nm and lateral sizes of 50–100 nm and located predominantly next to the lipid patches due to their release when the liposome is ruptured at the solid support surface. Nevertheless, these two techniques revealed the presence of a few larger particles in suspension, while the population was predominantly composed of smaller nanoparticles of interest.

To provide conclusive evidence regarding the effective colocalization of nanoparticles within the liposomal structures, we conducted additional experiments using confocal microscopy (Figure 9). Specific excitation/emission filters were selected for curcumin and NBD-cholesterol, a chemically modified fluorescent cholesterol incorporated into the liposomal formulation to create a traceable system. Figure 9 presents the confocal microscopy images of the carrier-in-carrier system (formulation LipoNBD-60). The three images correspond to the acquisitions performed using the specific filters for curcumin and NBD-cholesterol, along with their merged representation. In the merged image, the curcumin signal was assigned a yellow pseudocolor, while the fluorescent cholesterol signal was assigned a red pseudocolor. As a result, areas of overlap between the two components appear in orange, indicating their spatial co-localization within the system.

Additionally, we verified the presence of the bilayer within the formulation and assessed the eventual interaction between lipids and silk fibroin using FTIR (Figure 10 and Figure S7 and Table S2 in the Supporting Information). The strong absorbance of both loaded and empty liposomes at the wavenumbers, ν, 2918 and 2849 cm^{-1}, which corresponds to the vibrational bands of the CH_2 groups of lipids, confirms the presence of lipids in the sample with SFNPs. It is worth mentioning that even though SFNPs also absorb in this region, their absorbance is 20 times lower and does not contribute significantly to

Downloaded from pubs.acs.org/aamick/article-pdf/doi/10.1021/acsami.6c16066/69193937/am-2026-160662.pdf by guest on 15 November 2026

https://doi.org/10.1021/acsami.6c16066
ACS Appl. Mater. Interfaces XXXX, XXX, XXX–XXX

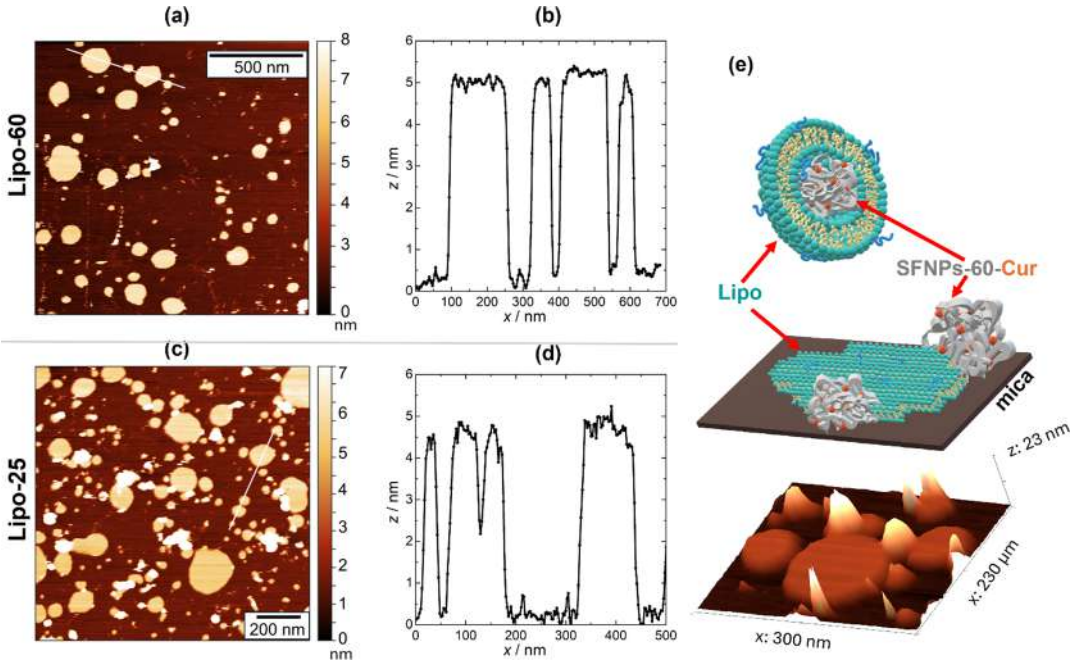


Figure 8. Representative AFM images and cross-section profiles for (a, b) Lipo-60 and (c, d) Lipo-25 measured in a liquid cell in water at 37 °C. (e) Schematic illustration of the liposome rupture on mica and 3D AFM height image of Lipo-25.

the total intensity. After SFNPs loading into the liposomes, the position of the CH_2 bands shifts to higher values of ν (2920 and 2851 cm^{-1}). This confirms that silk fibroin positively interacts with the lipid tails, as suggested by DLS, highlighting a possibly more tightly packed system upon mixing. Unloaded liposomes also absorb IR at the frequency of 1738 cm^{-1}, which corresponds to the excitation of the C–O groups, found in the phospholipid polar groups. The encapsulation of silk fibroin is witnessed by the appearance of absorbance bands in the Amide I and Amide II regions in the adsorption spectrum of the mixed system due to the presence of the protein. From the intensity and the position of these peaks, we can estimate the relative number of β-sheets and α-helices. We performed peak deconvolution using multiple peak analysis with a Gaussian function, and from the comparison of the calculated peak areas, we observed a 1.3-fold increase in the β-sheets content of SFNPs after their loading into liposomes, which is possibly a result of the silk fibroin interaction with the membrane. Thus, FTIR results stress that the lipid shell and the protein core of the formulation positively interact to form strongly coupled systems.

Thanks to the significant contrast for X-rays between the hydrophobic 'tales' and hydrophilic 'head' groups of phospholipids, water and proteins, we could characterize the carrier-in-carrier formulation structure at the nanoscale by SAXS (Figure 11). Empty liposomes show a well-pronounced membrane form factor in the region of transferred wave vectors q of ca. 1 nm^{-1} and exhibit a steep Bragg peak at $q = 0.97$ nm^{-1} (with a second-order repetition at $q = 1.94$ nm^{-1}). While the broad form factor shape is related to the membrane structural characteristics (density, composition, thickness), the presence of the Bragg peak indicates the multi-lamellarity of the liposomes. Specifically, the Bragg peak position corresponds to a distance in the direct space (related to the mean distance between repeating units, i.e., membranes + hydration water) of 6.5 nm. This was confirmed by extrusion of the liposomes; in particular, liposomes extruded through a polycarbonate membrane with a pore size of 200 nm do not exhibit Bragg peaks in the SAXS profile, but only the membrane form factor (Figure S8), indicating the unilamellarity of the extruded vesicles. After SFNPs encapsulation, the intensity of the membrane form factor weakens in the SAXS curves, while the scattering from SFNPs dominates the measured profiles. Nonetheless, the Bragg peak is preserved, albeit with lower intensity, indicating that even in the mixed system, more than one membrane layer surrounds the silk fibroin core. This property may facilitate controlled modulation of the curcumin release over time.

SAXS profiles have been modeled by a sequence of 3 concentric spherical shells with a protein core.[32,48] The model uses scattering length densities (SLD) of the core and each shell, as well as the core radius, R_{core}, and shell thicknesses, t_1, t_2, and t_3 (Figure 10c,d and Table S3 in the Supporting Information). For the liposome, core is the inner part of the vesicle filled with solvent and therefore indicates the size of the liposome and the SLD of the solvent, the first shell is the inner 'head' groups of the membrane (t_1, SLD_1), the second shell is the hydrophobic bilayer of the lipid 'tails' (t_2, SLD_2), and the third layer is the of the outer 'head' groups of the membrane (t_3, SLD_3). The SLD of the solvent was fixed to $9.44 \cdot 10^{-6}$ $Å^{-2}$ for all samples. Gaussian distribution for radius core polydispersity was implied (PDI = 0.3). The presented in Figure 11 fit of the SAXS curves of empty liposomes was obtained with an inner core radius $R_{core} = 80 \pm 2$ nm ($SLD_{core} = 9.47 \cdot 10^{-6}$ $Å^{-2}$), and shells with thicknesses of t_2 2.7 ± 0.1 nm for phospholipid tail bilayer (SLD = $8.4 \cdot 10^{-6}$ $Å^{-2}$), and $t_1 = 2.1$ and $t_3 = 2.0 \pm 0.1$ nm for lipid 'heads' ($SLD_1 = 10.5 \cdot 10^{-6}$ $Å^{-2}$ and $SLD_3 = 10.8 \cdot 10^{-6}$ $Å^{-2}$). The inner and outer shells are thicker in comparison to phospholipid bilayers due to the presence of polymer chains (PEG-2000). SAXS, consistently with DLS, evidenced that

Downloaded from pubs.acs.org/aamick/article-pdf/doi/10.1021/acsami.6c16066/6193937/am-2026-160662.pdf by guest on 15 November 2026

https://doi.org/10.1021/acsami.6c16066
ACS Appl. Mater. Interfaces XXXX, XXX, XXX–XXX

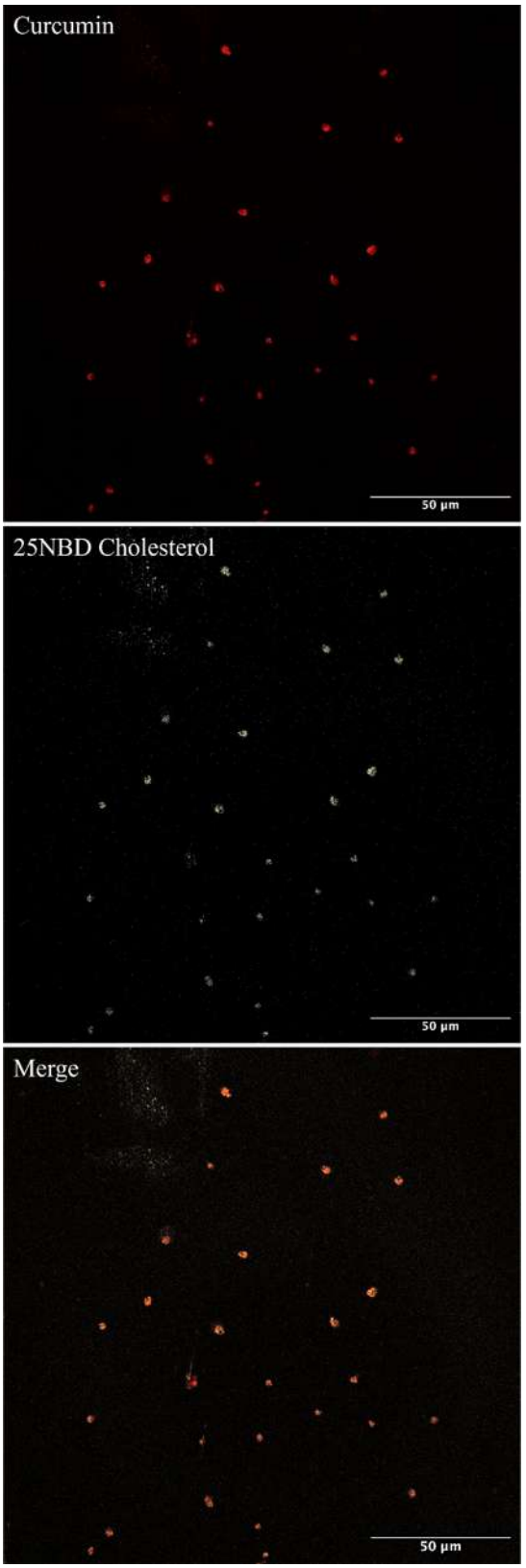


Figure 9. Confocal microscopy images of carrier-in-carrier LipoNBD-60 suspension obtained using different excitation/emission channels (specific for carrier-in-carrier components): curcumin (λ_{ex} 405 nm, λ_{em} 420–480 nm), 25-NBD cholesterol (λ_{ex} 543 nm, λ_{em} 565–575 nm), and merge image of the two channels (yellow and red for curcumin and 25-NBD, respectively).

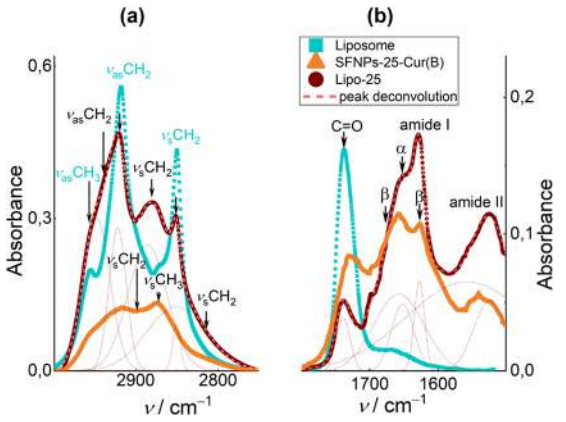


Figure 10. FTIR spectra of the SFNPs-25-Cur(B), liposomes, and formulation (Lipo-25) in the wavenumber region of (a) C–H vibrational bands (3000–2750 cm^{-1}) and (b) amide absorbance (1750–1500 cm^{-1}).

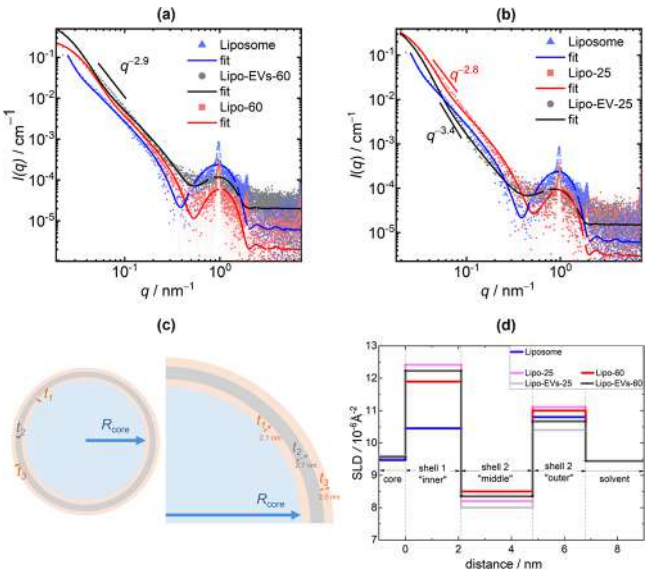


Figure 11. (a, b) Batch SAXS profiles of the formulations for SFNPs loaded to liposomes and fused with EVs measured in water at 37 °C. The SAXS curves were fitted by using the core multishell model. (c) Illustration of the core multishell model. (d) SLD profiles of the carrier-in-carrier system calculated using the core multishell model. The SLDs are plotted as a function of distance where 0 corresponds to the interface between core and inner shell.

loading of the SFNPs into liposomes leads to a decrease in the size of the formulation (R_{core} of 45 ± 4 nm), probably due to the sonication of the formulation for SFNPs encapsulation, while the thicknesses of the shells remain the same, underlying a non-disrupting effect of the fibroin core on the lipid bilayer. Moreover, changes in the SLDs of the core and all layers are observed upon mixing, with respect to the values obtained for the single components. The fact that the SLD of the core is modified upon mixing indicates that the lipid shell effectively encapsulated the silk fibroin particles, consistent with fluorescence measurements (Figure 9). The variation of the membrane SLD, related to the molecular composition and structuring of the bilayer, is in agreement with FTIR and serves

Downloaded from pubs.acs.org/aamick/article-pdf/doi/10.1021/acsami.6c16066/69193937/am-2026-160662.pdf by guest on 15 November 2026

https://doi.org/10.1021/acsami.6c16066
ACS Appl. Mater. Interfaces XXXX, XXX, XXX–XXX

as proof of positive interaction of the silk fibroin with lipids, slightly affecting their packing within the bilayer.

Thus, confocal microscopy and SAXS confirmed the localization of SFNPs within liposomes, while preserving the lipid bilayer structure. The results also suggest an additional positive interaction between silk fibroin and the lipid membrane, which may influence the properties of the lipid shell and contribute to formulation stability. At the solid-liquid interface, liposomes rupture and form a supported lipid bilayer, while the SFNPs are released but remain in close proximity to the lipid patches that may continue to mediate silk fibroin-lipid interactions, preventing the complete detachment of the SFNPs from the membrane. These observations suggest that the lipid-protein interaction may favor the localization of SFNPs within the liposomal structure and contribute to the stability of carrier-in-carrier system against degradation.

SFNPs with a Hybrid Lipid/EVs Shell

With the successful loading of SFNPs into liposomes and confirmation of the surrounding lipid bilayer, we further fused these formulations with EVs to enable the integration of membrane-associated constituents of mesenchymal stromal cell-derived EVs (proteinaceous and lipid-associated components) into the lipid shell of the nanoparticles. The overall shape of the SAXS profiles (Figure 11a,b) for the resulting formulation remained largely unchanged after fusion with EVs, underlying that EVs' inclusion into the surrounding lipid shell neither destabilizes the formulation structure nor decreases the number of lipid shells surrounding the protein core. Intriguingly, EVs' inclusion into the formulation leads to different variations: for the Lipo-EVs-60 formulation, the membrane form factor is modified as proof of EV components' inclusion into the synthetic lipid shell. On the other hand, for the Lipo-EVs-25 system, a SAXS curve slope increase at low q (below 0.3 nm^{-1}) is observed, suggesting increased system surface roughness, as if EV components did not deeply penetrate/tightly pack on the surrounding lipid membrane. We speculate that coupling at 60 vs 25 °C leads to distinct, though consistently favorable, protein-lipid interactions, which in turn affect the system's ability to incorporate additional components into the outer lipid shell. This difference could be strategically exploited to tailor interactions with specific target interfaces by modulating surface properties.

From SAXS data treatment, we observe the increase of the size of the formulation after fusion with EVs: R_{core} increases by 8 nm for both Lipo-EVs-25 and Lipo-EVs-60 in comparison to Lipo-25 and Lipo-60. The SLD_1 (inner shell) is also increased in comparison to unloaded liposomes, while SLD_2 (mid shell) and SLD_3 (outer shell) decreased (Figure 11c,d). The trend for SLD change for SFNPs loading is similar to that of EVs fusion (for SLD_{core}, SLD_1 and SLD_2 in comparison with liposome), suggesting that the nature of interaction, as well as the nature of molecules inserted into membranes, are similar. Based on these observations, we hypothesize that mostly proteins from EVs are inserted into the membrane and not lipids, although lipid exchange may still occur. Therefore, core multi-shell SAXS modeling quantitatively captures EV-induced changes in fitted shell SLD parameters together with a systematic increase in the fitted core radius, consistent with incorporation of additional components within and on the lipid shell.

Fractionation of the formulation showed the presence of a single peak in all elution profiles (detected by SAXS, MALS, and UV-vis) for the SFNPs loaded into liposomes with similar

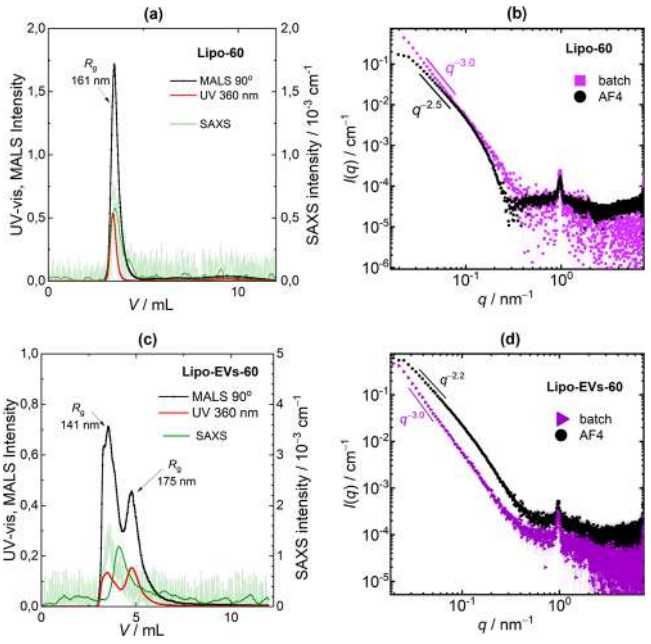


Figure 12. (a, c) MALS at scattering angle, θ, 90°, UV–vis at wavelength, λ, 360 nm, and SAXS elution profiles after AF4 fractionation. Light green lines are the experimental SAXS elution profiles, and dark green lines are the profiles smoothed using the Savitzky-Golay function. The R_g values were calculated from MALS; the error bars did not exceed 2%. (b, d) SAXS profiles of the sample measured in batch-mode and after fractionation using AF4 at the elution peak position.

R_g values for Lipo-25 and Lipo-60 (R_g of ca. 160 nm; Figure 12 and Figure S5). Moreover, no fractionation was observed in the comparison of the batch mode experiment and after AF4 for Lipo-25, indicating that most of the SFNPs are encapsulated into the liposomes (Figure S5). For Lipo-60, the encapsulation is less efficient since a significant difference in the scattering profiles of the batch and AF4 modes is observed (Figure 12); the scattering from non-encapsulated nanoparticles that remained in the solution gives a contribution to the scattering at low q in the batch-mode SAXS, while after fractionation, mostly the form factor of the liposome is observed. The elution profiles display a double peak upon fusion of the formulation with EVs with R_g of 140 nm and 170–200 nm. The second peak (R_g > 170 nm) possibly corresponds to the EVs, which is confirmed by the elution profile of the EVs alone (Figure S5 in the Supporting Information). Thus, an excess of EVs can be separated from the formulation by AF4. A clear difference is observed in the low q region between the formulations before and after EVs fusion. In particular, a shallower slope is observed after the fusion due to the contrast change of the membrane. AF4 fractionation further supports the EV inclusion after separating an excess EV population, while the EV-fused formulations display distinct low-q SAXS signatures compared to EV-free systems, consistent with a change in membrane contrast and interfacial organization. Moreover, the preservation of the form factor of NPs surrounded by a lipid shell after separation with AF4 indicates the stability of hybrid Lipid-EV/SFNP systems under flow conditions.

Downloaded from pubs.acs.org/aamick/article-pdf/doi/10.1021/acsami.6c16066/6193937/am-2026-160662.pdf by guest on 15 November 2026

https://doi.org/10.1021/acsami.6c16066
ACS Appl. Mater. Interfaces XXXX, XXX, XXX–XXX

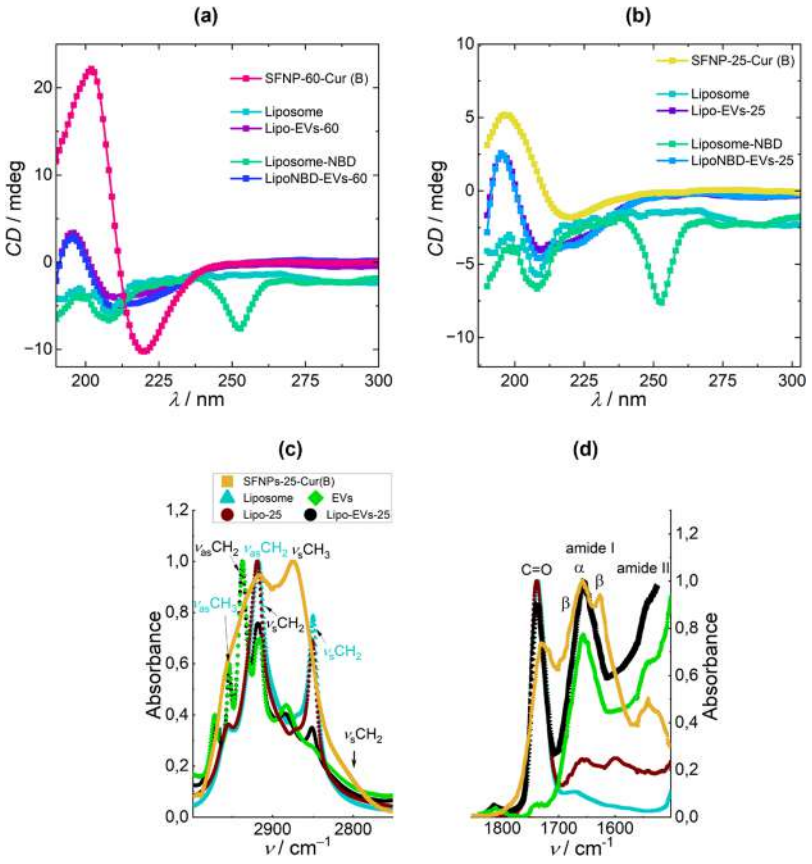


Figure 13. CD spectra of carrier-in-carrier with SFNPs prepared at (a) 60 °C and (b) 25 °C. The curves were fitted using the BeStSel method to determine the fractions of the secondary structure bases (Figure S9 and Table S4 in the Supporting Information). (c, d) Normalized FTIR spectra of the SFNPs and the formulations before and after fusion with EVs in the wavenumber region of C–H (3000–2750 cm^{-1}) vibrational bands and amide absorbance (1750–1500 cm^{-1}).

As expected for the observed positive interaction between lipid shell and protein core, CD measurements of the carrier-in-carrier formulations show that encapsulation of the SFNPs into liposomes is accompanied by a change in the secondary structure of silk fibroin (Figure 13 and Figure S9 and Table S4 in the Supporting Information). Loading the NPs into liposomes and further fusion with EVs leads to a significant decrease in the antiparallel secondary structure (Table 7) and the emergence of helical contributions that are absent in SFNP-only systems, supporting the presence of additional protein components attributable to EVs in the final formulation.

Notably, for the liposome with cholesterol-NBD, there is a strong negative ellipticity observed at 252 nm, which is probably related to the ordering of achiral NBD with preferred orientation within the lipid membrane. After NPs encapsulation and fusion with EVs, the minimum disappears due to the distortion of the cholesterol-NBD ordering and incorporation of the silk fibroin into the membrane. It is worth mentioning that no significant difference in SAXS profiles and FTIR of the liposomes containing cholesterol-NBD and the ones without a fluorescent label was observed (see Figures S8–S10), so the fluorescence label does not affect the properties of the membrane, and the findings could be applied to the formulation without the NBD label as well. The interaction of silk fibroin with the lipid membrane, together with the contribution of EV-associated proteins to the measured ellipticity, leads to a decrease in the relative

Table 7. Fractions of α-Helices, Parallel and Antiparallel β-sheets, Turns, and Other Secondary Structure Basis Components Obtained from Fitting CD Spectra of Formulations Using the BeStSel Method[24,a]

	fraction, %				
sample	helix	antiparallel	parallel	turn	others
Lipo-EVs-60	6.3 ± 0.1	28.3 ± 0.2	4.0 ± 0.1	15.0 ± 0.2	46.4 ± 0.3
Lipo-EVs-25	4.8 ± 0.1	28.6 ± 0.3	2.8± 0.1	15.5 ± 0.2	48.3 ± 0.5
LipoNBD-EVs-60	9.7 ± 0.2	25.7 ± 0.2	5.4 ± 0.2	14.3 ± 0.1	44.9 ± 0.4
LipoNBD-EVs-25	7.0 ± 0.2	27.1 ± 0.3	3.5 ± 0.1	15.3 ± 0.2	47.2 ± 0.4
SFNP-60-Cur(B)	0	50.4 ± 0.5	20.1 ± 0.2	4.8 ± 0.2	24.7 ± 0.3
SFNP-25-Cur(B)	0	41.6 ± 0.3	0	11.7 ± 0.2	46.7 ± 0.5

[a]The uncertainties of the fitting parameters are fitting errors.

https://doi.org/10.1021/acsami.6c16066
ACS Appl. Mater. Interfaces XXXX, XXX, XXX–XXX

Downloaded from pubs.acs.org/aamick/article-pdf/doi/10.1021/acsami.6c16066/69193937/am-2026-160662.pdf by guest on 15 November 2026

content of antiparallel β-sheets. FTIR provides an independent readout of membrane alteration after EV fusion, showing shifts of the CH_3 and CH_2 vibrational bands (2954, 2920, and 2851 cm^{-1}) as well as of the C–O vibrational band (1740 cm^{-1}) (Figure 13 and Figure S7 and Table S5 in the Supporting Information), that are sensitive to lipid packing and headgroup environment, consistent with insertion/association of EV-derived components.

The SAXS, CD, and FTIR data suggest that EV-derived components modify the outer shell by changing membrane packing, shell contrast, and surface organization. Such changes may affect how the hybrid carrier interacts with biological interfaces, for example by altering surface roughness, hydration, steric accessibility, and the presentation of EV-associated proteins.

Imaging of the formulations using AFM proved the localization of the nanoparticles within the hybrid liposome (Figure 14). The deposition of carrier-in-carrier system onto mica leads to the rupture of hybrid lipid-EV vesicular structure; however, SFNPs remained enclosed within the liposome even after the rupture of the lipid-EV shell, which may result from more robust silk fibroin-membrane interactions that anchor it inside in comparison to the ones without EVs. The cross-section analysis of the AFM images shows the presence of the liposomes fused onto mica (relatively flat, laterally extended regions) with lateral size of 150–250 nm and the membrane thickness of 4–5 nm (Figure S6 in the Supporting Information), with SFNPs (brighter protrusions) located within the liposomal patches with the height of 20–30 nm and the size of 100–150 nm. The bilayer thicknesses are slightly lower than the ones calculated from SAXS, possibly because of the difference in the conformation of PEG in the outer and inner shells of the liposome, depending on the curvature of the membrane The sizes of the vesicles and SFNPs correspond to the measurements obtained from DLS and AF4-SAXS. We hypothesize that the fusion with EVs stabilizes the entrapment and incorporation of SFNPs within the liposome, which enhances the prospects of hybrid systems for drug delivery applications.

The in vitro curcumin release profiles of carrier-in-carrier systems confirm that the encapsulation of SFNPs into liposomes and liposome/vesicles significantly affects the release kinetics (Figure 15). The interaction between the fibroin core and lipid shell slows down the curcumin release with respect to the SFNPs alone.

All formulations exhibited a biphasic release profile, characterized by a rapid release during the first 24 h, followed by a sustained, plateauing phase through 72 h. Both the silk fibroin

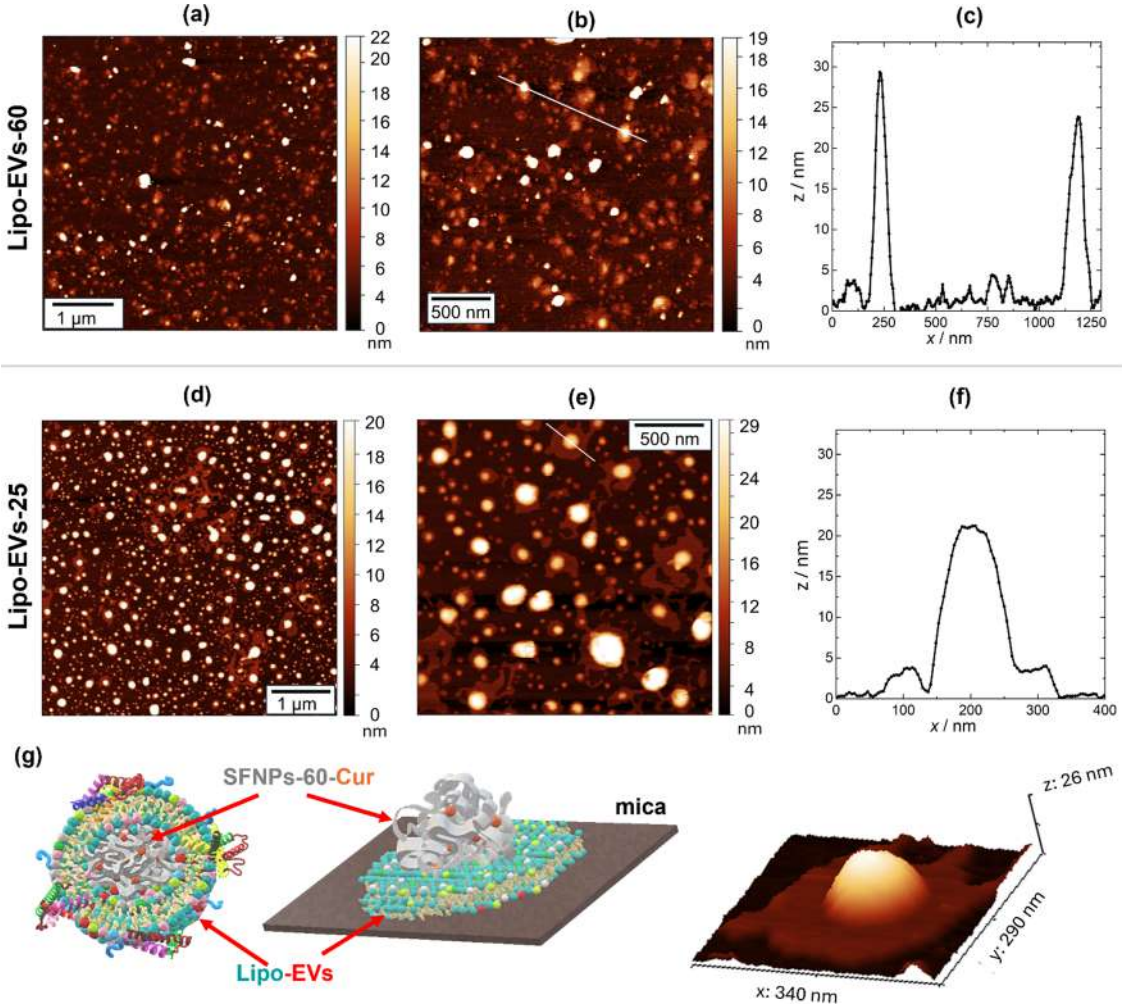


Figure 14. Representative AFM images of formulations and cross-section profiles of the SFNPs loaded into liposomes and fused with EVs: (a–c) Lipo-EVs-60 and (d–f) Lipo-EVs-25. (g) Schematic illustration of Lipo-EVs-25 rupture on mica surface and 3D AFM image.

Downloaded from pubs.acs.org/aamick/article-pdf/doi/10.1021/acsami.6c16066/6919393/am-2026-160662.pdf by guest on 15 November 2026

https://doi.org/10.1021/acsami.6c16066
ACS Appl. Mater. Interfaces XXXX, XXX, XXX–XXX

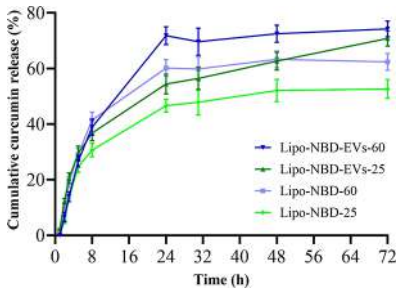


Figure 15. In vitro curcumin release profile from the SFNPs with lipid and hybrid lipid/EV shell. Data are expressed as mean values and standard deviations obtained by the analysis of at least three independent batches for each considered formulation.

degumming temperature (25 vs 60 °C) and the composition of the lipidic shell (with or without EVs) modulated the release kinetics (Figure 15). The formulations prepared with fibroin solubilized at 60 °C exhibited a higher cumulative drug release compared to those processed at 25 °C, similarly to the SFNPs without lipid shell (Figure 6).

This behavior could be attributed to structural changes within the silk fibroin core induced by thermal treatment; the higher processing temperature promotes a structural transition toward a more compact, highly hydrophobic, crystalline β-sheet structure as confirmed by SAXS and FTIR for SFNPs (Figure 4 and Table 6 and Figure S1). The structural compaction might reduce the internal loading spaces within the SFNP core or alter the partitioning coefficient of the hydrophobic curcumin, effectively driving a larger fraction of the drug toward the outer lipid shell or interfacial regions, thereby facilitating its dissolution and release into the medium.

Furthermore, the fusion of EVs into the lipidic shell significantly improved the percentage of curcumin released after 72 h (One-way ANOVA, $p < 0.05$); in particular, Lipo-NBD-EVs-60 and Lipo-NBD-EVs-25 totally released 74.2 ± 2.8% and 70.8 ± 2.7% of curcumin, respectively, without significant differences between the two groups (ANOVA, $p > 0.05$). Hybrid systems prepared without the EVs fusion presented a lower cumulative curcumin release: 62.4 ± 3.0% and 52.6 ± 2.3% for Lipo-NBD-60 and Lipo-NBD-25, respectively.

Comparing the carrier-in-carrier systems (Figure 15) and the SFNPs (Figure 6) in terms of curcumin release, no differences were observed during the initial 8–12 h, and all formulations exhibited a comparable release rate. From 24 h onward, we observed an effect of the lipidic shell that markedly slowed down and reduced the curcumin release compared to the uncoated SFNPs. At 48 h, uncoated SFNPs reached 90–100% cumulative release, while the hybrid systems plateaued at significantly lower levels (ANOVA, $p < 0.05$), reducing the overall release to approximately 50–70%, depending on the formulation (Figure 15). These results confirmed the data previously published by other authors in which a lipid shell around polymeric nanoparticles reduced the drug release from the core,[49−51] due to the decreased porosity of the nanoparticles with the lipid shell and/or entrapment of the curcumin within the lipid membrane.

Overall, these results establish the carrier-in-carrier system as a sequentially engineered platform in which each formulation step addresses a specific structural requirement (Figure 1). Fibroin solubilization controls the aggregation state and compactness of the SFNP core; curcumin loading defines cargo–matrix interactions and release behavior; liposome encapsulation provides a stabilizing membrane shell; and EV fusion further modifies shell composition, packing, and permeability. Together, these findings show that both the internal protein matrix and the external lipid/EV interface can be tuned to modulate the final architecture and release performance of the hybrid nanocarrier.

The developed hybrid architecture (Figure 1) provides functional and practical implications; in particular, the use of SFNPs dramatically increases the payload of hydrophobic molecules. Unlike monolithic nanocarriers, our systems offer dual-gate control due to the presence of both the lipid shell and crystalline core; the hybridization of the system by the inclusion of EVs in the shell represents a functional strategy that is intended to reduce immune recognition and exploit the natural tropism of EVs. The AF4-MALS and SAXS data in this work were specifically used to demonstrate that the particles maintain their integrity without undergoing significant aggregation. This is a crucial "practical advantage" for administration, where particle instability often leads to embolization or rapid clearance. Furthermore, these advanced techniques, by enabling the investigation of subtle interfacial properties of the system, not only demonstrate that production methods, and consequently the hybrid systems, are reproducible - a fundamental aspect for clinical applications – but can also be profitably used as a cell-free strategy for the design of innovative delivery systems tailored to specific needs.

■ CONCLUSIONS

Here, we demonstrated a carrier-in-carrier strategy in which silk fibroin nanoparticles (SFNPs) are structurally tuned and then incorporated into an EV–liposome hybrid shell to obtain a modular nanocarrier for hydrophobic cargo delivery. The key requirement for this system is the ability to control both the internal protein matrix and the external membrane interface, since both determine colloidal stability, cargo retention, and release behavior.

We first showed that fibroin solubilization conditions in LiBr act as an upstream process parameter controlling SFNP aggregation state, compactness, and surface roughness. Curcumin was efficiently encapsulated, with encapsulation efficiency of approximately 76–85% and drug loading up to approximately 6% w/w. The resulting release profiles confirmed that the SFNP matrix provides a controllable protein-based reservoir for hydrophobic cargo.

We then demonstrated that SFNPs can be incorporated into PEGylated DPPC/cholesterol liposomes to form a carrier-in-carrier architecture. SAXS/AF4-enabled analysis, supported by FTIR, CD, confocal microscopy and AFM, showed that the lipid shell remains structurally organized and interacts with the silk fibroin core. Fusion with mesenchymal stromal cell-derived EVs introduced EV-derived membrane-associated components into the shell while preserving the overall nanosystem architecture. The EV-containing shell further modified membrane packing and permeability, contributing to the modulation of curcumin release.

Overall, this study establishes a process-informed framework for the rational design of hybrid lipid/EV–silk nanocarriers. By linking fibroin solubilization, SFNP nanostructure, shell engineering, and release performance, the work provides a structure-based proof of concept for reproducible carrier-in-carrier systems in

Downloaded from pubs.acs.org/aamick/article-pdf/doi/10.1021/acsami.6c16066/6193937/am-2026-160662.pdf by guest on 15 November 2026

https://doi.org/10.1021/acsami.6c16066
ACS Appl. Mater. Interfaces XXXX, XXX, XXX–XXX

which the protein core and the biomimetic external interface can be tuned independently.

■ ASSOCIATED CONTENT

Supporting Information

The Supporting Information is available free of charge at https://pubs.acs.org/doi/10.1021/acsami.6c16066.

Additional data and analysis of CD and FTIR spectra, AF4-MALS and AF4-SAXS elution profiles, SAXS profiles, AFM images of SFNPs and carrier-in-carrier systems, SAXS profile of EVs, and gyration radii and molecular masses distributions (DOCX)

■ AUTHOR INFORMATION

Corresponding Authors

Sara Perteghella – *Department of Drug Sciences, University of Pavia, Pavia 27100, Italy;* orcid.org/0000-0003-1128-7636; Email: sara.perteghella@unipv.it

Valeria Rondelli – *Department of Medical Biotechnology and Translational Medicine, Università degli Studi di Milano, Segrate 20054, Italy;* orcid.org/0000-0001-8409-9025; Email: valeria.rondelli@unimi.it

Authors

Luca Randi – *Department of Drug Sciences, University of Pavia, Pavia 27100, Italy*

Anastasiia Murmiliuk – *Department of Medical Biotechnology and Translational Medicine, Università degli Studi di Milano, Segrate 20054, Italy*; Present Address: UR Molecular Systems, Department of Chemistry, University of Liège, Liège, 4000, Belgium; orcid.org/0000-0001-6775-2563

Elia Bari – *Department of Pharmaceutical Sciences, University of Piemonte Orientale, Novara 28100, Italy*

Laura Catenacci – *Department of Drug Sciences, University of Pavia, Pavia 27100, Italy*

Milena Sorrenti – *Department of Drug Sciences, University of Pavia, Pavia 27100, Italy*

Guillaume Gilliard – *Department of Medical Biotechnology and Translational Medicine, Università degli Studi di Milano, Segrate 20054, Italy*; Present Address: Unité de génie enzymatique et cellulaire, Université de Picardie Jules Vernes, Amiens, 80039, France

Alice Piccinini – *Department of Medical Biotechnology and Translational Medicine, Università degli Studi di Milano, Segrate 20054, Italy*; Present Address: School of Pharmacy, University of Camerino, Camerino (Macerata), 62032, Italy

Gouranga Manna – *ESRF, The European Synchrotron, Grenoble 38000, France*

Clement Blanchet – *Hamburg Unit, European Molecular Biology Laboratory, Hamburg 22607, Germany*

Melissa Ann Gräwert – *Hamburg Unit, European Molecular Biology Laboratory, Hamburg 22607, Germany*

Aleksi Sutinen – *Hamburg Unit, European Molecular Biology Laboratory, Hamburg 22607, Germany*

Baohu Wu – *Jülich Centre for Neutron Science (JCNS) at Heinz Maier-Leibnitz Zentrum (MLZ), Forschungszentrum Jülich, Garching 85748, Germany;* orcid.org/0000-0002-1291-8965

Luca Puricelli – *Area Science Park, Padriciano, Trieste 34149, Italy*

Loredana Casalis – *Elettra-Sincrotrone Trieste, Basovizza, Trieste 34149, Italy*

Maria Cristina Bonferoni – *Department of Drug Sciences, University of Pavia, Pavia 27100, Italy*

Complete contact information is available at: https://pubs.acs.org/doi/10.1021/acsami.6c16066

Author Contributions

[$]L.R. and A.M. contributed equally to this work. L.R.: data curation, investigation, visualization, and writing–original draft, review, and editing; A.M.: data curation, formal analysis, funding acquisition, investigation, methodology, visualization, and writing–original draft, review, and editing; E.B.: funding acquisition, investigation, and writing–review and editing; L. Catenacci: supervision, validation, and writing–review and editing; M.S.: supervision, validation, and writing–review and editing; G.G.: investigation and writing–review and editing; A.P.: investigation and writing–review and editing; G.M.: formal analysis and writing–review and editing; C.B.: formal analysis, investigation, and writing–review and editing; M.A.G.: data curation, investigation, and writing–review and editing; A.S.: formal analysis, investigation, and writing–review and editing; B.W.: formal analysis and writing–review and editing; L.P.: formal analysis, investigation, and writing–review and editing; L. Casalis: investigation and writing–review and editing. M.C.B.: formal analysis, supervision, validation, and writing–review and editing; S.P.: conceptualization, funding acquisition, methodology, project administration, resources, supervision, validation, visualization, and writing–original draft, review, and editing; V.R.: conceptualization, funding acquisition, methodology, project administration, resources, supervision, validation, visualization, and writing–original draft, review, and editing.

Notes

The authors declare no competing financial interest.

■ ACKNOWLEDGMENTS

This research was funded by "European Union – Next Generation EU Mission 4 Componente 1 (PRIN 2022 ID: 20223SM7T2 - Anastasia CUP: F53D23004980001, CUP G53D23003300001)". This work was also supported by the Department of Excellence 2023-2027, Project "SCALE UP" funded by the Italian Ministry of University and Research (MUR), Department of Molecular Biotechnology, and Translational Medicine of the University of Milano. We acknowledge the European Synchrotron Radiation Facility (ESRF, proposal SC-5603 and LS-3423) for the provision of synchrotron radiation facilities. The raw data from ID02 beamline at ESRF are available at https://doi.esrf.fr/10.15151/ESRF-ES-1837447272 and https://doi.esrf.fr/10.15151/ESRF-ES-1925860640. We acknowledge the Partnership for Soft-Condensed Matter (PSCM) laboratories in Grenoble for the use of laboratories and instrumentation. The synchrotron SAXS data were collected at beamline P12 operated by EMBL Hamburg at the PETRA III storage ring (DESY Hamburg, Germany) within the proposals SAXS-1436 and SAXS-1364. This work benefited from access to the P12 beamline (EMBL Hamburg), an Instruct-ERIC center. Financial support was provided by Instruct-ERIC (PID: 37692 and 33670). G.G. and V.R.

Downloaded from pubs.acs.org/aamick/article-pdf/doi/10.1021/acsami.6c16066/6193937/am-2026-160662.pdf by guest on 15 November 2026

acknowledge the support of Next Generation EU PNRR Mission 4 Component 2 Investment 1.1 (project EXTREME, CUP: G53D23007030001). A.P. and V.R. acknowledge the funding received from the Italian Ministry of University and Research, PRIN2020 Project 2020MHL8S9 "MITHOS". This work has also been partially funded by the European Union - NextGenerationEU within the project PNRR "PRP@CERIC" IR0000028.

The authors thank Massimo Boiocchi, Patrizia Vaghi, Amanda Oldani of Centro Grandi Strumenti (University of Pavia), and Dr. Gloria Milanesi of the Biology and Biotechnology Department (University of Pavia) for their support and assistance in TEM and confocal microscopy analyses. The authors acknowledge the assistance of Pierre Lloria from the Partnership for Soft Condensed Matter (PSCM) at the ESRF and Dr. Ludmila Mee from ISIS Neutron and Muon Source in sample preparation and pre-characterization. The authors are also thankful to Dr. Ekaterina Kostyurina (Ludwig-Maximilians University) for her assistance with sample preparation for SAXS experiments, as well as Dr. Sergey K. Filippov (DWI – Leibniz Institute for Interactive Materials) and Dr. Dmytro Soloviov (European Molecular Biology Laboratory) for their assistance with AF4-SAXS measurements.

REFERENCES

(1) Kaltbeitzel, J.; Wich, P. Protein-based Nanoparticles: From Drug Delivery to Imaging, Nanocatalysis and Protein Therapy. *Angew. Chem., Int. Ed.* **2023**, *62* (44), No. e202216097.

(2) Murmiliuk, A.; Iwase, H.; Kang, J.; Mohanakumar, S.; Appavou, M.; Wood, K.; Almásy, L.; Len, A.; Schwärzer, K.; Allagaier, J.; et al. Polyelectrolyte-protein synergism: pH-responsive polyelectrolyte/insulin complexes as versatile carriers for targeted protein and drug delivery. *J. Colloid Interface Sci.* **2024**, *665*, 801–813.

(3) Ma, Y.; Canup, B.; Tong, X.; Dai, F.; Xiao, B. Multi-Responsive Silk Fibroin-Based Nanoparticles for Drug Delivery. *Front. Chem.* **2020**, *8*, No. 585077.

(4) Reizabal, A.; Costa, C.; Pérez-Alvarez, L.; Vilas-Vilela, J.; Lanceros-Méndez, S. Silk Fibroin as Sustainable Advanced Material: Material Properties and Characteristics, Processing, and Applications. *Adv. Funct. Mater.* **2023**, *33* (3), No. 2210764.

(5) Asakura, T. Structure of Silk I (Bombyx mori Silk Fibroin before Spinning) -Type II β-Turn, Not α-Helix-. *Molecules* **2021**, *26* (12), No. 3706.

(6) Cheng, G.; Wang, X.; Wu, M.; Wu, S.; Cheng, L.; Zhang, X.; Dai, F. Insignificant Difference in Biocompatibility of Regenerated Silk Fibroin Prepared with Ternary Reagent Compared with Regenerated Silk Fibroin Prepared with Lithium Bromide. *Polymers* **2022**, *14* (18), No. 3903.

(7) Crivelli, B.; Perteghella, S.; Bari, E.; Sorrenti, M.; Tripodo, G.; Chlapanidas, T.; Torre, M. L. Silk nanoparticles: from inert supports to bioactive natural carriers for drug delivery. *Soft Matter* **2017**, No. C7SM01631J.

(8) Shaidani, S.; Jacobus, C.; Sahoo, J.; Harrington, K.; Johnson, H.; Foster, O.; Cui, S.; Hasturk, O.; Falcucci, T.; Chen, Y.; et al. Silk Nanoparticle Synthesis: Tuning Size, Dispersity, and Surface Chemistry for Drug Delivery. *ACS Appl. Nano Mater.* **2023**, *6* (20), 18967–18977.

(9) Perteghella, S.; Sottani, C.; Cocce, V.; Negri, S.; Cavicchini, L.; Alessandri, G.; Cottica, D.; Torre, M. L.; Grignani, E.; Pessina, A. Paclitaxel-Loaded Silk Fibroin Nanoparticles: Method Validation by UHPLC-MS/MS to Assess an Exogenous Approach to Load Cytotoxic Drugs. *Pharmaceutics* **2019**, *11* (6), No. 285.

(10) Bao, S.; Yang, X.; Reis, R.; Xiao, B.; Kundu, S.; Duan, L. Synthesis and application of silk fibroin nanoparticles for drug delivery. *Commun. Mater.* **2026**, *7* (1), No. 1108.

(11) Wang, H.; Zhang, Y.; Wei, Z. Dissolution and processing of silk fibroin for materials science. *Crit. Rev. Biotechnol.* **2021**, *41* (3), 406–424.

(12) Cunha, J.; Latocheski, E.; Fidalgo, A.; Gerola, A.; Marin, C.; Ribeiro, A. Core-shell hybrid liposomes: Transforming imaging diagnostics and therapeutic strategies. *Colloids Surf., B* **2025**, *251*, No. 114597.

(13) Zeng, H.; Guo, S.; Ren, X.; Wu, Z.; Liu, S.; Yao, X. Current Strategies for Exosome Cargo Loading and Targeting Delivery. *Cells* **2023**, *12* (10), No. 1416.

(14) Liu, W.; Wu, L.; Chen, C.; Zheng, H.; Gao, J.; Lu, Z.; Li, M. Lipid-hybrid cell-derived biomimetic functional materials: A state-of-the-art multifunctional weapon against tumors. *Mater. Today Bio* **2023**, *22*, No. 100751.

(15) Carissimi, G.; Lozano-Pérez, A.; Montalbán, M.; Aznar-Cervantes, S.; Cenis, J.; Víllora, G. Revealing the Influence of the Degumming Process in the Properties of Silk Fibroin Nanoparticles. *Polymers* **2019**, *11* (12), No. 2045.

(16) Jacobus, C.; Shaidani, S.; Tonies, E.; Soehnlein, R.; Chen, Y.; Kaplan, D. Functional Performance of Silk Nanoparticles for Oral Drug Delivery. *ACS Appl. Mater. Interfaces* **2026**, *18* (22), 31046–31060.

(17) Cho, H. J. The effect of dissolution condition on the yield, molecular weight, and wet- and electro-spinnability of regenerated silk fibroins prepared by LiBr aqueous solution. *Int. J. Ind. Entomol.* **2010**, *20* (2), 7.

(18) Perteghella, S.; Crivelli, B.; Catenacci, L.; Sorrenti, M.; Bruni, G.; Necchi, V.; Vigani, B.; Sorlini, M.; Torre, M. L.; Chlapanidas, T. Stem cell-extracellular vesicles as drug delivery systems: New frontiers for silk/curcumin nanoparticles. *Int. J. Pharm.* **2017**, *520* (1–2), 86–97.

(19) Seib, F.; Jones, G.; Rnjak-Kovacina, J.; Lin, Y.; Kaplan, D. pH-Dependent Anticancer Drug Release from Silk Nanoparticles. *Adv. Healthcare Mater.* **2013**, *2* (12), 1606–1611.

(20) Crivelli, B.; Bari, E.; Perteghella, S.; Catenacci, L.; Sorrenti, M.; Mocchi, M.; Farago, S.; Tripodo, G.; Prina-Mello, A.; Torre, M. L. Silk fibroin nanoparticles for celecoxib and curcumin delivery: ROS-scavenging and anti-inflammatory activities in an in vitro model of osteoarthritis. *Eur. J. Pharm. Biopharm.* **2019**, *137*, 37–45.

(21) Bari, E.; Tartara, F.; Cofano, F.; Di Perna, G.; Garbossa, D.; Perteghella, S.; Sorlini, M.; Mandracchia, D.; Giovannelli, L.; Gaetani, P.; et al. Freeze-Dried Secretome (Lyosecretome) from Mesenchymal Stem/Stromal Cells Promotes the Osteoinductive and Osteoconductive Properties of Titanium Cages. *Int. J. Mol. Sci.* **2021**, *22* (16), No. 8445.

(22) Bari, E.; Perteghella, S.; Di Silvestre, D.; Sorlini, M.; Catenacci, L.; Sorrenti, M.; Marrubini, G.; Rossi, R.; Tripodo, G.; Mauri, P.; et al. Pilot Production of Mesenchymal Stem/Stromal Freeze-Dried Secretome for Cell-Free Regenerative Nanomedicine: A Validated GMP-Compliant Process. *Cells* **2018**, *7* (11), No. 190.

(23) Oelichmann, J. Surface and depth-profile analysis using FTIR spectroscopy. *Fresenius Z. Anal. Chem.* **1989**, *333* (4–5), 353–359.

(24) Micsonai, A.; Wien, F.; Bulyáki, É.; Kun, J.; Moussong, É.; Lee, Y.; Goto, Y.; Réfrégiers, M.; Kardos, J. BeStSel: a web server for accurate protein secondary structure prediction and fold recognition from the circular dichroism spectra. *Nucleic Acids Res.* **2018**, *46* (W1), W315–W322.

(25) Narayanan, T.; Sztucki, M.; Van Vaerenbergh, P.; Léonardon, J.; Gorini, J.; Claustre, L.; Sever, F.; Morse, J.; Boesecke, P. A multipurpose instrument for time-resolved ultra-small-angle and coherent X-ray scattering. *J. Appl. Crystallogr.* **2018**, *51*, 1511–1524.

(26) Narayanan, T.; Sztucki, M.; Zinn, T.; Kieffer, J.; Homs-Puron, A.; Gorini, J.; Van Vaerenbergh, P.; Boesecke, P. Performance of the time-resolved ultra-small-angle X-ray scattering beamline with the Extremely Brilliant Source. *J. Appl. Crystallogr.* **2022**, *55*, 98–111.

(27) Michael, S. SAXSutilities2: a graphical user interface for processing and analysis of Small-Angle X-ray Scattering data (1.024). **2021**.

(28) Blanchet, C.; Spilotros, A.; Schwemmer, F.; Graewert, M.; Kikhney, A.; Jeffries, C.; Franke, D.; Mark, D.; Zengerle, R.; Cipriani, F.; et al. Versatile sample environments and automation for biological solution X-ray scattering experiments at the P12 beamline (PETRA III, DESY). *J. Appl. Crystallogr.* **2015**, *48*, 431–443.

Downloaded from pubs.acs.org/aamick/article-pdf/doi/10.1021/acsami.6c16066/6193937/am-2026-160662.pdf by guest on 15 November 2026

(29) Franke, D.; Kikhney, A.; Svergun, D. Automated acquisition and analysis of small angle X-ray scattering data. *Nucl. Instrum. Methods Phys. Res., Sect. A* **2012**, *689*, 52–59.
(30) Schmidt, P. Small-Angle Scattering Studies of Disordered, Porous and Fractal Systems. *J. Appl. Crystallogr.* **1991**, *24*, 414–435.
(31) Hurd, A.; Schaefer, D.; Martin, J. Surface and Mass Fractals in Vapor-Phase Aggregates. *Phys. Rev. A* **1987**, *35* (5), 2361–2364.
(32) Feigin, L. A.; Svergun, D. I. *Structure analysis by Small-Angle X-Ray and Neutron Scattering*; Springer: New York, NY, **1987**.
(33) Doucet, M.; Cho, J. H.; Alina, G.; Attala, Z.; Bakker, J.; Bouwman, W.; Butler, P.; Campbell, K.; Cooper-Benun, T.; Durniaj, C.; et al. SasView version 5.0.4. **2021**.
(34) Bressler, I.; Kohlbrecher, J.; Thunemann, A. SASfit: a tool for small-angle scattering data analysis using a library of analytical expressions. *J. Appl. Crystallogr.* **2015**, *48*, 1587–1598.
(35) Da Vela, S.; Bartels, K.; Franke, D.; Soloviov, D.; Gräwert, T.; Molodenskiy, D.; Kolb, B.; Wilhelmy, C.; Drexel, R.; Meier, F.; et al. AF4-to-SAXS: expanded characterization of nanoparticles and proteins at the P12 BioSAXS beamline. *J. Synchrotron Radiat.* **2025**, *32*, 971–985.
(36) Graewert, M.; Wilhelmy, C.; Bacic, T.; Schumacher, J.; Blanchet, C.; Meier, F.; Drexel, R.; Welz, R.; Kolb, B.; Bartels, K.; et al. Quantitative size-resolved characterization of mRNA nanoparticles by in-line coupling of asymmetrical-flow field-flow fractionation with small angle X-ray scattering. *Sci. Rep.* **2023**, *13* (1), No. 42274.
(37) Manalastas-Cantos, K.; Konarev, P.; Hajizadeh, N.; Kikhney, A.; Petoukhov, M.; Molodenskiy, D.; Panjkovich, A.; Mertens, H.; Gruzinov, A.; Borges, C.; et al. ATSAS 3.0: expanded functionality and new tools for small-angle scattering data analysis. *J. Appl. Crystallogr.* **2021**, *54*, 343–355.
(38) Panjkovich, A.; Svergun, D. CHROMIXS: automatic and interactive analysis of chromatography-coupled small-angle X-ray scattering data. *Bioinformatics* **2018**, *34* (11), 1944–1946.
(39) Shaikh, J.; Ankola, D. D.; Beniwal, V.; Singh, D.; Kumar, M. N. V. R. Nanoparticle encapsulation improves oral bioavailability of curcumin by at least 9-fold when compared to curcumin administered with piperine as absorption enhancer. *Eur. J. Pharm. Sci.* **2009**, *37* (3-4), 223–230.
(40) Mandracchia, D.; Trapani, A.; Perteghella, S.; Sorrenti, M.; Catenacci, L.; Torre, M. L.; Trapani, G.; Tripodo, G. pH-sensitive inulin-based nanomicelles for intestinal site-specific and controlled release of celecoxib. *Carbohydrate Polym.* **2018**, *181*, 570–578.
(41) Yewale, C.; Baradia, D.; Patil, S.; Bhatt, P.; Amrutiya, J.; Gandhi, R.; Kore, G.; Misra, A. Docetaxel loaded immunonanoparticles delivery in EGFR overexpressed breast carcinoma cells. *J. Drug Delivery Sci. Technol.* **2018**, *45*, 334–345.
(42) Necas, D.; Klapetek, P. Gwyddion: an open-source software for SPM data analysis. *Cent. Eur. J. Phys.* **2012**, *10* (1), 181–188.
(43) Ta, W.; Li, X.; Song, J.; Hua, R.; Zheng, Y.; Lu, W. Customizable Dual-Fluorescent Nanoparticles for Tracing and Quantifying of Cell Transport. *Int. J. Nanomed.* **2023**, *18*, 1823–1834.
(44) He, Y.; Zhang, N.; Li, W.; Jia, N.; Chen, B.; Zhou, K.; Zhang, J.; Chen, Y.; Zhou, C. N-Terminal Domain of Bombyx mori Fibroin Mediates the Assembly of Silk in Response to pH Decrease. *J. Mol. Biol.* **2012**, *418* (3-4), 197–207.
(45) Stuhrmann, H. B. Small-angle scattering of X-rays. *Prog. Cryst. Growth Charact. Mater.* **1989**, *18*, 1–19.
(46) Higgins, J. S.; BenoÎt, H. C. *Polymers and Neutron Scattering*; Oxford University Press, **1998**.
(47) King, S. Small-angle Neutron Scattering. In *Modern Techniques for Polymer Characterisation*, Pethrick, R. A.; Dawkins, J. V. Eds.; Wiley, **1999**; pp 416.
(48) Kline, S. Reduction and analysis of SANS and USANS data using IGOR Pro. *J. Appl. Crystallogr.* **2006**, *39*, 895–900.
(49) Gajbhiye, K.; Salve, R.; Narwade, M.; Sheikh, A.; Kesharwani, P.; Gajbhiye, V. Lipid polymer hybrid nanoparticles: a custom-tailored next-generation approach for cancer therapeutics. *Mol. Cancer* **2023**, *22* (1), 1849.
(50) Krishnamurthy, S.; Vaiyapuri, R.; Zhang, L.; Chan, J. Lipid-coated polymeric nanoparticles for cancer drug delivery. *Biomater. Sci.* **2015**, *3* (7), 923–936.
(51) Hassan, A.; Ramadan, E.; Kristó, K.; Regdon, G. J.; Sovány, T. Lipid-Polymer Hybrid Nanoparticles as a Smart Drug Delivery System for Peptide/Protein Delivery. *Pharmaceutics* **2025**, *17* (6), No. 797.

Downloaded from pubs.acs.org/aamick/article-pdf/doi/10.1021/acsami.6c16066/6919393937/am-2026-160662.pdf by guest on 15 November 2026

https://doi.org/10.1021/acsami.6c16066
ACS Appl. Mater. Interfaces XXXX, XXX, XXX–XXX